Editors' Suggestion

# Fabrication and test of a 6-tesla-class high-temperature superconducting dipole magnet at 4.2 K

Dmytro Abraimov,[1] Diego Arbelaez,[2] Lucas Brouwer,[2] Jean-François Croteau,[2] Joseph DiMarco,[3] Paolo Ferracin,[2,*] William B. Ghiorso,[2] Hugh C. Higley,[2] Mariusz Juchno,[2] Andy Lin,[2] Thomas Lipton,[2] Linqing Luo,[2] Maxim Marchevsky,[2] Marek Mosat,[2] Michael Naus,[2] Ryan Norris,[2] Ian Pong,[2] Soren O. Prestemon,[2,†] Kyle Radcliff,[4] José Luis Rudeiros Fernández,[2] GianLuca Sabbi,[2] Anjana Saravanan,[2] Tengming Shen,[2] Reed Teyber,[2] Marcos Turqueti,[2] Giorgio Vallone,[2] Danko van der Laan,[4,5,‡] Timothy Villabona,[2] Xiaorong Wang,[2,§] Jeremy D. Weiss,[4,5] Yuxin Wu,[2] and Yufan Yan[2]

[1]*Applied Superconductivity Center, National High Magnetic Field Laboratory Florida State University, Tallahassee, Florida 32310, USA*
[2]*Lawrence Berkeley National Laboratory, Berkeley, California 94720, USA*
[3]*Fermi National Accelerator Laboratory, Batavia, Illinois 60510, USA*
[4]*Advanced Conductor Technologies LLC, Boulder, Colorado 80301, USA*
[5]*University of Colorado, Boulder, Colorado 80309, USA*

(Received 15 March 2026; accepted 16 July 2026; published 14 August 2026)

Superconducting magnets enable energy-frontier accelerators by generating strong magnetic fields to steer and focus the particles. Although high-temperature superconductors such as $REBa_2Cu_3O_x$ (REBCO, RE = rare earth) hold a strong potential for generating a higher magnetic field than Nb-Ti and $Nb_3Sn$, the associated magnet and conductor technology for accelerator applications is still in its infancy. The U.S. Magnet Development Program is developing REBCO magnet technology in collaboration with industry. Here we report an experiment of making a dipole magnet called C3 using commercial high-temperature superconducting CORC® wires. The magnet, following a canted $\cos\theta$ design, generated a dipole field of 5.99 T at 4.2 K in its clear aperture of 65 mm at 6.795 kA when a resistive voltage of 105 μV appeared across one of the coils in the magnet. The stored energy was 53 kJ at the peak field. The magnet showed no degradation in the current-carrying capability at 4.2 K after the thermal cycle. We report on the detailed design, fabrication, and performance of the C3 magnet that can be of interest to potential users of this emerging technology. We also discuss issues and research needs to inform future REBCO magnet development. The experiment represented another step to addressing if the high-temperature superconducting accelerator magnet technology can increase the discovery capability of future particle accelerators.

DOI: 10.1103/4nhs-bkwh

## I. INTRODUCTION

Superconducting magnet technology, despite its complex nature, has enabled energy-frontier particle accelerators since the first application of Nb-Ti magnets in the CERN Intersecting Storage Rings complex in 1980 and the full-scale accelerator realization in the Tevatron at FNAL in 1983 [1–4]. With a maximum achievable dipole field of 10 T, the Nb-Ti technology achieved its prominence in the Large Hadron Collider (LHC) at CERN, where a landmark discovery of the Higgs boson particle was made in 2012 [2,5]. After decades of development, $Nb_3Sn$ magnet technology, capable of generating a dipole magnetic field of 16–17 T, is rising with the first application in the interaction-region quadrupole magnets for the High-Luminosity LHC [6–9].

What can high-temperature superconducting (HTS) materials bring to the table?

Bi-2212 and $REBa_2Cu_3O_x$ (REBCO, RE = rare earth) conductors, two commercial HTS conductors, can remain superconducting in a magnetic field higher than 20 T at 4.2 K [10–13]. Specifically, a REBCO coil developed at NHMFL recently generated a solenoid field of 17.6 T within a background field of 31.1 T, surpassing the previous

*Contact author: pferracin@lbl.gov
†Contact author: soprestemon@lbl.gov
‡Contact author: danko@advancedconductor.com
§Contact author: xrwang@lbl.gov

record of 14.4 T in the same background field [14,15]. Therefore, we expect the HTS magnet technology to eventually further boost the discovery capability of future circular colliders [16–18]. For the same reason, HTS materials are expected to help achieve higher energy gain and plasma density in compact magnetic-confinement fusion machines to generate electricity at scale [19,20].

The critical temperatures for Bi-2212 and REBCO are between 85 and 95 K, significantly higher than those of Nb-Ti and $Nb_3Sn$. They thus enhance the thermal margin of HTS magnets at 4.2 K, which is attractive for applications with a strong heat load on the magnets [21,22].

Thanks to their high irreversibility field, REBCO conductors can operate at elevated temperatures like 20 K [10,23–25]. While this reduces absolute current capacity, it vastly improves thermal stability via increased heat capacity. Additionally, operating at elevated temperatures improves cryogenic Carnot efficiency, providing a thermodynamic advantage that supports the sustainability goals for future colliders outlined in the 2023 P5 report [26].

Despite these attractive features, we do not yet have a REBCO magnet technology that can generate a dipole field above the limit of $Nb_3Sn$ due to several technical challenges.

REBCO conductors are produced in tape form to achieve a useful current-carrying capacity [27]. Although single-tape magnet winding is possible [28–31], high-field low-inductance accelerator magnets favor a compact conductor that can carry a current on the order of 10 kA, necessitating a cable composed of multiple REBCO tapes. Several REBCO cable concepts exist [12], but the community has not yet converged on a definitive architecture.

The ceramic superconducting layer in a REBCO tape, a few μm thick so far, is brittle. The composite tape is prone to delamination under shear loads, despite its exceptional mechanical resilience under compression transverse to the broad surface of the tape. Bending without degrading REBCO tapes can be a constraint when making a multipolar magnet [32].

The very properties that make REBCO attractive can also become a hindrance. Massive critical currents combined with millimeter-scale filaments generate strong magnetization, which deteriorates field quality and drives up hysteresis losses. Simultaneously, REBCO's exceptional thermal stability works against quench protection systems; it conceals local hot spots, leaving the magnet highly susceptible to undetected thermal damage.

The magnet community has started addressing these challenges. Centered at CERN, the European collaboration is spearheading the development of REBCO technology with a series of coherent programs ranging from the earlier EuCARD programs [33–35] to the current High Field Magnets R&D (HFM) program [36].

The EuCARD programs contributed significant results and experiences to the community, including, but not limited to, a dipole field of 5.4 T at 4.2 K in a racetrack magnet using a four-tape REBCO cable [35,37,38], a dipole field of 4.5 T at 4.2 K with an aperture of 40 mm using an aligned-block design and REBCO Roebel cable [35,39,40], and a dipole field of 1.2 T at 4.5 K in a $\cos\theta$ dipole magnet limited by an underperforming coil [38,41].

As part of the HFM program, CERN started a racetrack-coil program [42]. A common-coil configuration using four racetrack coils recently generated 5.4 T in the 20-mm-diameter apertures as part of a road map toward 14 T and beyond [43].

Record dipole fields were also generated using the no-insulation and metal-insulated REBCO designs. Tsinghua University achieved a dipole field of 5.02 T in a 34-mm clear bore of a block-type dipole magnet with flared ends at 4.2 K [44]. The Institute of High Energy Physics developed a REBCO common coil using six racetrack coils that achieved the record 7.6 T in a 25-mm aperture at 4.2 K [45]. A metal-insulated racetrack magnet from the HFM program generated 5.1 T at 4.2 K at CEA Saclay using a 4-mm-wide REBCO tape [46].

Following the 2014 P5 recommendations, the U.S. Department of Energy established the Magnet Development Program (MDP) in 2016 to advance high-field superconducting magnets for future particle accelerators. A core mandate of the MDP is to demonstrate high-field HTS magnet technology [47,48].

On the Bi-2212 front, the MDP partnered with industry to develop a common-coil type magnet that achieved 4.7 T at 4.2 K [49]. The magnet consisted of two racetrack coils wound with high-performance Bi-2212 Rutherford cable [50,51]. The magnet showed neither quench training nor degradation from intentional quenches or thermal cycles.

On the REBCO front, the MDP focuses on the round-conductor architectures sourced from two domestic manufacturers [52,53]. To define conductor requirements and prove round REBCO wire feasibility, the program has fabricated and tested diverse magnet topologies, including Conductor on Molded Barrel [54], canted $\cos\theta$ (CCT) [55] and uni-layer [56,57]. Parallel efforts by external groups have also successfully integrated round REBCO cables into accelerator magnets [58,59].

Here we report on a short dipole magnet called C3 that was developed following the earlier magnets C1 [60] and C2 [61]. The C3 magnet generated a dipole field of 5.99 T using HTS CORC® wires at 4.2 K during the 2025 test campaign. To our knowledge, this was the first time that an HTS magnet, with a field-quality design relevant for particle accelerators, reached such a dipole field.

We used the C3 dipole short model to evaluate several critical engineering and physics metrics. Specifically, we needed to assess the REBCO conductor development implemented for C3 and determine how effectively round CORC® wire integrates with CCT coil design and fabrication. Magnet performance was a primary focus, requiring us to measure the maximum current capacity, the peak dipole field, and the overall magnetic-field quality, stability, and reproducibility. We also aimed to quantify energy loss during field sweeping and validate the performance of the electrical joints. Ultimately, this model was built to identify any fundamental showstoppers or future development needs required for a REBCO CCT magnet to hit the 8 to 10 T range currently dominated by Nb-Ti magnet technology.

We are also curious if the emerging REBCO magnet technology can be useful for the readers of this paper. If not, what features are missing? We look forward to your feedback.

The paper is organized as the following. Section II introduces the CORC® wire, followed by detailed overviews of the magnet design and fabrication in Secs. III and IV. Section V outlines the instrumentation and measurement protocols. We then present the experimental data, covering the 4.2 K CORC® wire performance in Sec. VI, overall magnet performance in Sec. VII, and field quality in Sec. VIII. Sections IX and X quantify the energy loss and electrical termination resistance, respectively. Finally, we discuss the results, issues, and development needs in Sec. XI.

## II. CORC® WIRES

The C3 magnet used a round wire called the Conductor on Round Core (CORC®) wire, produced by Advanced Conductor Technologies (ACT) LLC [52]. The wire has 30 REBCO tapes helically wrapped around a Cu core (Fig. 1). The wire has an outer diameter (OD) of 3.7–3.8 mm and can be bent to a radius of 30 mm with less than 10% degradation in the current-carrying capability of the wire [62,63]. Liquid lubricant was introduced during the cabling process to improve the bending performance of the CORC® wire.

The CORC® wire features a factory-applied polyester heat-shrink insulation jacket with a nominal radial thickness of 25 μm. This insulation completely encapsulates the conductor, providing electrical isolation from both the adjacent turns and the metallic mandrels.

SuperPower Incorporation produced the commercial REBCO tapes for the CORC® wire used in the C3 magnet. The critical current of the constituent tape, “HM” type, has been optimized for applications at low temperatures and in high magnetic fields. The 2-mm-wide tape has a minimum critical current of 350 A at 6 T, 4.2 K when the applied magnetic field is perpendicular to the broad surface of the tape [63]. Table I shows the nominal parameters for the CORC® wire used in the C3 magnet.

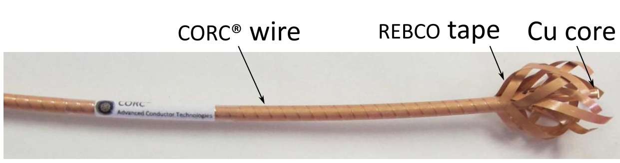


FIG. 1. A close-up view of the CORC® wire used in the C3 magnet.

TABLE I. Nominal parameters of a single CORC® wire used in the C3 magnet.

| Parameters | Unit | Value |
|---|---|---|
| REBCO tape type | [⋯] | SuperPower HM |
| Number of tapes | [⋯] | 30 |
| Layers of tapes | [⋯] | 12 |
| Tapes per layer | [⋯] | 2–3 |
| Tape width | mm | 2 |
| Tape thickness | μm | 45 |
| Substrate thickness | μm | 30 |
| Cu thickness per tape side | μm | 5 |
| Diameter of Cu core | mm | 2.54 |
| Polyester jacket thickness | μm | 25 |
| Cu to non-Cu ratio | [⋯] | 1.0 |

ACT fabricated six lengths of CORC® wire, one for each layer of the C3 magnet. The total length of the CORC® wires was 145 m, consuming a total of 7.5 km long REBCO tapes.

The MDP procured the wires using three orders placed between February 2019 and March 2020. ACT delivered the orders between August and December 2023. The 3-year lead time was largely driven by implementing the process required for producing high-quality HM REBCO tapes at volume.

Compared to flat-stacked tapes, round REBCO cables suffer from two fundamental inefficiencies. First, twisting the tapes into a helix significantly increases the total length of material required. Second, the central core dilutes the overall conductor current density, $J_{overall}$, defined as the current per unit cross-sectional area of the conductor, including the insulation. A higher $J_{overall}$ reduces the conductor usage when generating the same dipole field [64,65]. Table III in Sec. VI quantifies the $J_{overall}$ for the CORC® wires used in the C3 magnet.

Nevertheless, the round REBCO cable has a few features that are worthy of consideration. It is less constrained in the bending direction, accommodating various magnet designs and geometries that require complex three-dimensional bending. Additionally, their current capacity remains highly independent of external field orientations, simplifying the overall magnet design. With the cabling process separated from the magnet winding process, the conductor vendor and magnet winder can each do one thing and do it well.

## III. MAGNET DESIGN

The C3 magnet followed the CCT design introduced by Meyer and Flasck in 1970 [66]. Since then, several groups have further developed and extended the concept [67–76].

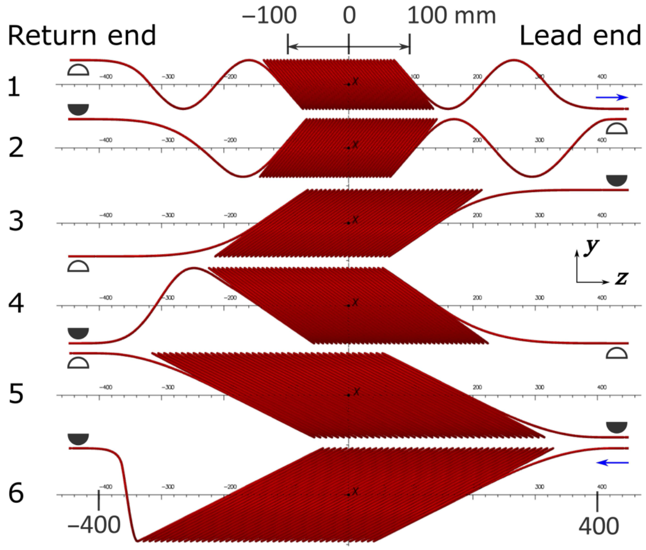


FIG. 2. The layout of the individual layers projected to the *y-z* plane. The layers are electrically in series. Two facing half-circles denote an interlayer electrical joint. Current flows from the Layer 6 lead end and exits from the Layer 1 lead end. The scale is in mm.

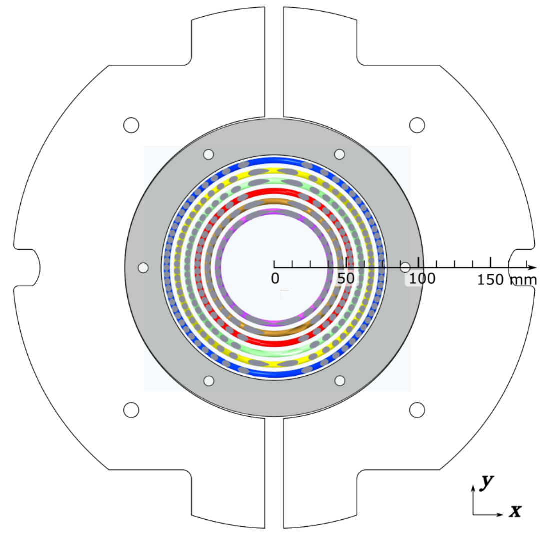


FIG. 3. The view of the six nested layers projected to the *x-y* plane. Also shown are the aluminum shell next to Layer 6 and the iron yoke outside the shell. The scale is in mm.

The CCT design has a few features attractive for high-field accelerator magnet applications. First, the conductor is embedded in a metal mandrel that intercepts the accumulation of electromagnetic forces on the conductor, which is important for strain-sensitive conductors such as REBCO. Second, the conductor path is related to the current-density distribution to generate specific field components and to meet the requirements on field quality [72].

TABLE II. Main parameters for the C3 magnet.

| Parameters | Unit | Layer 1 | 2 | 3 | 4 | 5 | 6 | Shell |
|---|---|---|---|---|---|---|---|---|
| ID | mm | 65.0 | 85.2 | 99.4 | 113.6 | 127.8 | 142.0 | 156.2 |
| Wire-center diameter | mm | 78.1 | 92.3 | 106.5 | 120.7 | 134.9 | 149.1 | [⋯] |
| OD at mandrel ends | mm | 84.1 | 98.3 | 112.5 | 126.7 | 140.9 | 155.1 | 207.0 |
| Radial gap between the neighboring layers | mm | | | | 0.55 | | | |
| Spar thickness | mm | 4.5 | 1.5 | 1.5 | 1.5 | 1.5 | 1.5 | [⋯] |
| Number of turns | [⋯] | | | 40 | | | | [⋯] |
| Nominal layer length | mm | | | | 900 | | | |
| Fabricated wire length | m | 15.0 | 17.0 | 22.0 | 25.0 | 31.5 | 34.5 | [⋯] |
| Used wire length | m | 13.0 | 15.1 | 20.1 | 22.7 | 29.4 | 32.6 | [⋯] |
| Wire manufacturing date, 2023 | mmdd | 0829 | 0926 | 1003 | 1025 | 1101 | 1213 | [⋯] |
| Coil winding date, 2024 | mmdd | 0322 | 0514 | 0730 | 0820 | 0918 | 1016 | [⋯] |
| Wire-to-coil time interval | months | 7 | 8 | 10 | 10 | 11 | 10 | [⋯] |
| Nominal wire diameter | mm | 3.72 | 3.72 | 3.73 | 3.70 | 3.73 | 3.77 | [⋯] |
| Groove diameter | mm | | | 4.1 | | | | [⋯] |
| Measured gap between wires at the midplane | mm | 0.32 | 0.29 | 0.30 | 0.36 | 0.55 | 0.47 | [⋯] |
| Layer weight, including conductors | kg | 14.5 | 12.1 | 13.9 | 15.7 | 17.5 | 19.3 | 35.3 |
| Wire tilt angle at the midplane | degree | 50 | −50 | −35 | 35 | 27 | −27 | [⋯] |
| Minimum bending radius of the wire center line | mm | 30 | 35 | 30 | 35 | 30 | 35 | [⋯] |
| Dipole field at 6.8 kA, analytical, without iron | T | | | 5.15 | | | | [⋯] |
| Layer contribution, analytical, without iron | [⋯] | 13.7% | 13.7% | 17.4% | 17.4% | 18.9% | 18.9% | [⋯] |
| Dipole field at 6.8 kA, Opera, without iron | T | | | 5.08 | | | | [⋯] |
| Layer contribution, Opera, without iron | [⋯] | 13.9% | 14.0% | 17.7% | 17.9% | 18.3% | 18.2% | [⋯] |
| Dipole field at 6.8 kA, Opera, with iron | T | | | 5.99 | | | | [⋯] |
| Peak conductor field at 6.8 kA, Opera, with iron | T | 6.19 | 6.18 | 5.83 | 5.49 | 4.95 | 4.40 | [⋯] |
| Magnet inductance at 6.8 kA | mH | | | 2.3 | | | | [⋯] |
| Magnet stored energy at 6.8 kA | kJ | | | 53 | | | | [⋯] |

The CCT design has shortcoming, too [77]. It uses more conductors than the $\cos\theta$ or block design to generate the same dipole field. It is challenging to machine a CCT mandrel for an accelerator magnet that is 10–15 m long, although assembly of segmented mandrels can be a solution [78–80].

The CCT design has been applied to dipole accelerator magnets using Bi-2212 [81–83] and $Nb_3Sn$ [84–86]. It has also been applied to magnets for medical applications [78,79,87–89], corrector magnets for the High-Luminosity LHC [90], and other accelerator magnet applications [91]. A. Godeke and colleagues at NHMFL and ACT first applied CORC® conductors in a CCT configuration [92].

The C3 magnet consists of six nested layers. Figure 2 shows the conductor layout for each layer. There are 40 turns of CORC® wires in each layer, generating a dipole and solenoid field in the aperture due to the tilted winding. The six layers are divided into three pairs. The two layers of each pair tilt in an opposite way to cancel the solenoid component and to double the dipole component once assembled.

When projected to the $x$-$y$ plane, the conductor layout of the assembled magnet becomes six concentric circles (Fig. 3).

We used aluminum bronze 954 for the mandrels and aluminum alloy 6061-T6 for the shell. Surrounding the center part of the magnet is an iron yoke (Figs. 3 and 9) composed of 16 laminated 1018 steel segments, each featuring a nominal thickness of 25.4 mm and an outer diameter of 362 mm to clear the test cryostat envelope. To accommodate differential thermal contraction during cryogenic cooldown, the inner diameter (ID) of the iron yoke is machined to be larger than the outer diameter of the aluminum shell, establishing a deliberate radial clearance at room temperature (Fig. 3). The iron yoke design followed that of the $Nb_3Sn$ CCT5 magnet [85].

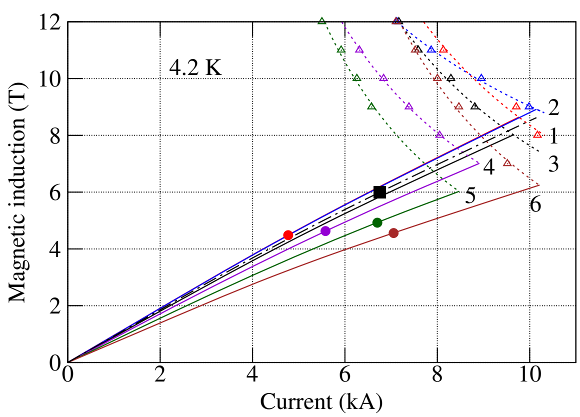


FIG. 4. Expected performance limit for each layer of the C3 magnet. Solid lines: The peak magnetic induction transverse to the longitudinal axis of the CORC® wire in each layer. Dashed lines: The performance limit of the conductor in each layer, as determined by a voltage criterion of 5 μV. Open triangles: Measured conductor performance at 4.2 K. The dot-dashed line: The expected dipole field in the magnet aperture. Section VI has more details on the conductor performance. The black square: The maximum dipole field generated during the test. The solid circles mark the current and peak induction on the conductor when the layer voltage reached 5 μV during the test. Section VII B has more details on the measured magnet performance at 4.2 K.

Table II lists the main parameters of the C3 magnet. The trace iron content within the aluminum bronze mandrels was excluded from the field calculations.

The short-sample limit of the C3 magnet at 4.2 K was determined by the peak magnetic induction transverse to the longitudinal axis of the conductor and the critical current of the witness sample of each layer (Fig. 4).

According to Fig. 4, we expect the C3 magnet to generate a dipole field of 7.34 T at 4.2 K when Layer 5 conductor first reaches its short-sample limit at 8.475 kA. At a dipole field of 6 T, the load-line margin is designed to be 30% for Layer 1, which has the highest magnetic field in the conductor.

## IV. MAGNET FABRICATION

Prior to the fabrication of the C3 magnet, a subscale prototype designated C3a was made. The C3a magnet was geometrically identical to C3 but featured only three turns per layer [63], serving as the baseline vehicle to validate and practice the layer-nesting and winding procedures.

Following the prototype protocols, all six layers of the C3 magnet were wound using an automated Winder Mark 2 platform [63] (a visual demonstration of the winding is available in this YouTube video [93]). Figure 5 illustrates the continuous positioning of the CORC® wire within the precision-machined mandrel grooves.

After the coil winding, voltage-tap wires and distributed fiber optic sensors, DFOS, were co-wound along the CORC®

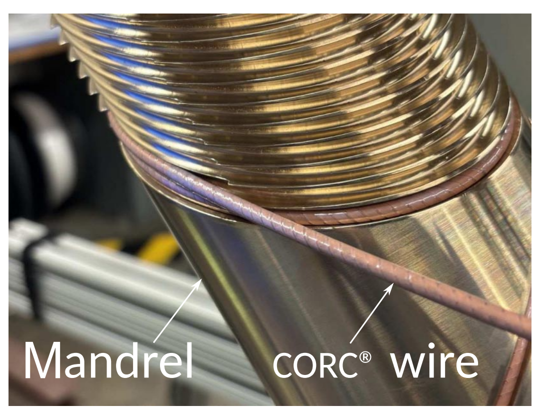


FIG. 5. CORC® wire settles in the groove machined on Layer 2 mandrel.

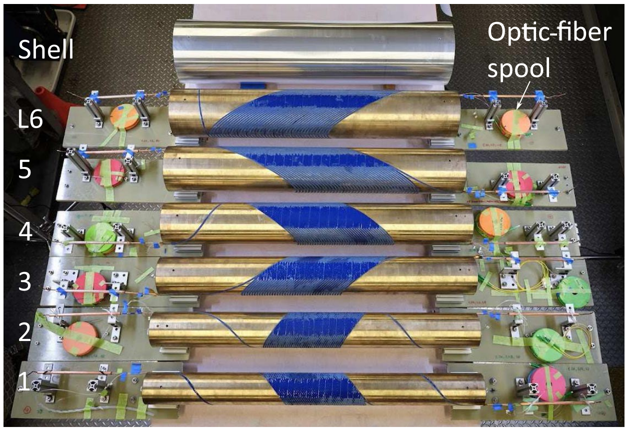


FIG. 6. The six layers and aluminum shell before assembly.

wire. The sensors were mechanically locked into the mandrel channels via a manual application of filled cryogenic epoxy, Stycast 2850 MT. Figure 6 shows the six completed layers and the aluminum shell prior to final assembly.

Figure 7 shows the duration of each major step to fabricate individual layers. It took about 140 to 180 h to complete one layer, including the mandatory room-temperature curing cycles of the epoxy. Two or three staff members worked together for about 4 h a day on the coil fabrication and 77 K test.

Final magnet assembly was achieved by sequentially nesting the inner mandrel layers within the outer structures. Figure 8 presents the cross-sectional end view of the integrated magnet assembly after full nesting inside the aluminum shell. Layer centering and alignment tolerances are detailed in Ref. [63].

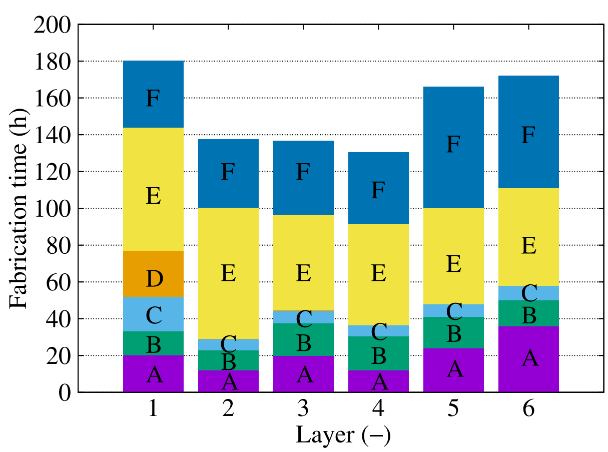


FIG. 7. The duration of the major steps to fabricate individual layers. Step A: Polish the mandrel. B: Wind coil and install electrical terminations. C: Install voltage-tap wires and optic fibers. D: Test at 77 K before applying Stycast, Layer 1 only. E: Apply and cure Stycast. F: Test at 77 K after applying Stycast.

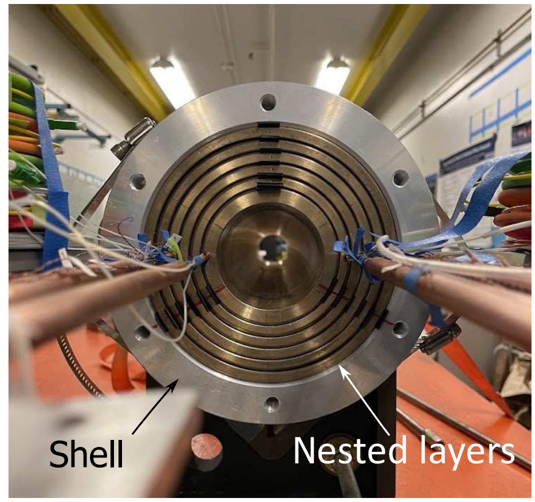


FIG. 8. The end view of the C3 magnet.

Following mechanical assembly, the remaining concentric radial boundaries between adjacent layers were filled using Stycast 2850 FT to establish continuous mechanical coupling and a uniform thermal conduction path between the layers and the aluminum shell. Postimpregnation electrical-isolation testing showed a reasonable dielectric baseline, with conductor-to-mandrel and mandrel-to-mandrel insulation resistances uniformly exceeding 60 MΩ across all layers. The six concentric layers were subsequently integrated into a series circuit via low-resistance interlayer splice terminations, fabricated according to the protocols reported in Ref. [63].

The two halves of the iron yoke were assembled around the shell using high-strength structural bolts tensioned against compliant Belleville spring washers to a maximum torque of 22.6 N m (200 in lb), maintaining an intentional mating gap at the yoke split boundaries in the pole region of the magnet (Fig. 3). Structural strain tracking during yoke fastening was monitored via the integrated DFOS arrays on the aluminum shell and Layer 6. More details on the fiber response will be reported elsewhere. Figure 9 shows the assembled magnet.

We had several issues when making the C3 magnet. (i) Layer 1 Wire Straightening: The CORC® wire electrically shorted to the mandrel during winding. Approximately 0.5 turns of the CORC® wire was unwound to address the short. The unwinding partially straightened the wire segment that was already bent, which risked degrading the REBCO tapes and was not advised by the vendor. The wire was then wound again into the mandrel. (ii) Layer 4 Conductor Kink: Early in the winding, the conductor prematurely unspooled and bound against an adjacent threaded framing rod, inducing a localized high-strain, sharp bend. Leveraging the length safety margin of the conductor batch, the winding was successfully restarted from the opposite end of the spool, routing the kinked segment into the lead-end

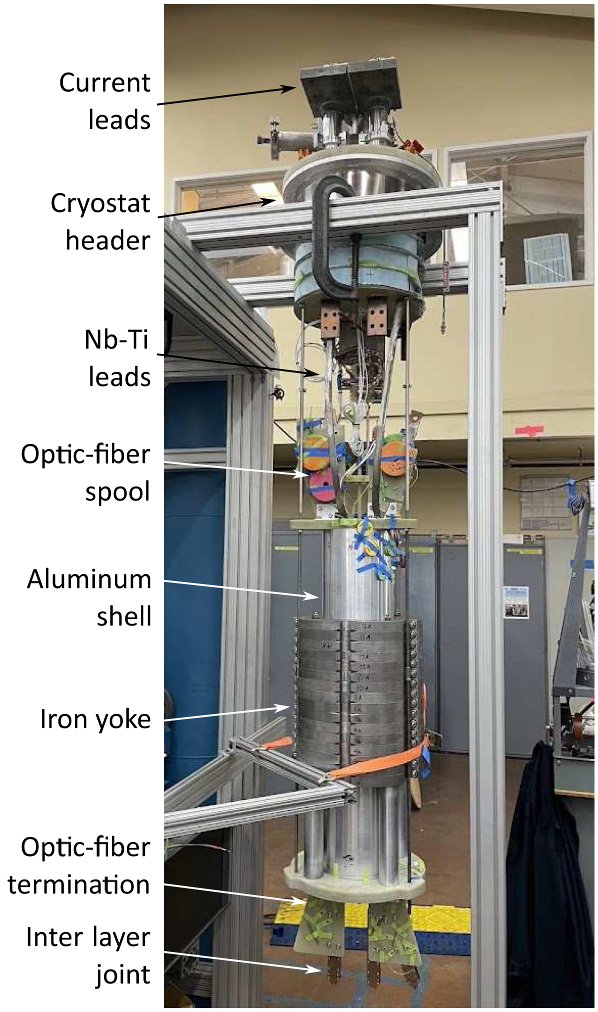


FIG. 9. The C3 magnet during the test preparation.

electrical termination block. (iii) Layer 4 Structural Fixture Failure: During the epoxy curing, one end of the support shaft failed and fell but was fortunately arrested by an auxiliary safety stand. The impact, however, induced a minor rotational displacement of the mandrel relative to the support shaft, subjecting the rigid lead CORC® wires to localized bending deformation. Visual documentation of the Layer 4 anomalies is compiled in Appendix A. (iv) Epoxy Aperture Infiltration: During the filling of the interlayer radial spaces, liquid Stycast infiltrated and filled approximately 50% of the central magnet aperture across its total axial length. Following the initial 4.2 K test, this monolithic block of cured epoxy was mechanically extracted from the inner bore using a specialized custom cutting tool detailed in Ref. [94].

## V. MEASUREMENT PROTOCOL AND EXPERIMENTAL SETUP

The current-carrying capability of the magnet was evaluated via layer-by-layer voltage diagnostics. Voltage

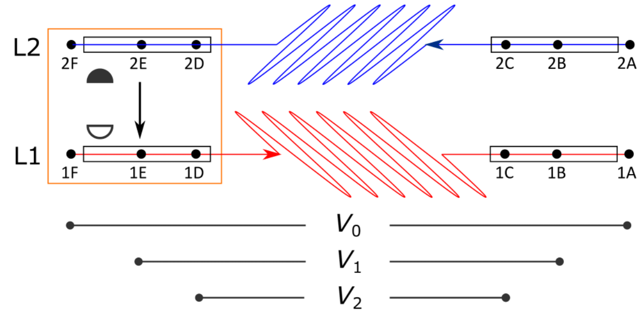


FIG. 10. Voltage-tap locations in the terminations of the CORC® wire. Only the first two layers are shown as an example. The orange box indicates the interlayer joint. The arrow shows the direction of the magnet current.

taps were embedded inside the electrical terminations [63]. Their locations are illustrated in Fig. 10. Three pairs of the voltage taps across each layer were used. Here we report $V_2$ data to minimize the effect of termination resistance. The resistance of the interlayer joint between Layers 1 and 2 was measured using the voltage between Taps 2D and 1D.

Prior to final magnet assembly, the voltage across each layer was measured as a function of the current in liquid nitrogen at 77 K to quantify the critical current of each layer and to assess if the layer can be used for further magnet assembly. Layer 1 was measured before and after applying the Stycast to verify the impact of epoxy impregnation on the coil's performance. Layer voltage signals were measured using Keithley 2182A nanovolt meters.

The magnet current was ramped to a preset target value to keep the resistive voltage across individual layers below around 100 μV, for both the 77 and 4.2 K tests. Upon reaching the target level, the magnet current was ramped down to zero. This operational constraint ensured the magnet remained bounded within an unquenched regime, minimizing the risk of conductor degradation due to thermal runaway and simplifying the protection of the magnet if the magnet was not driven to quench.

The experimental campaign for the C3 magnet had two discrete cryogenic test phases (Fig. 11). Phase I, with the Stycast in the aperture, evaluated the central dipole field component using a calibrated cryogenic Hall probe (F.W. Bell BHA-921) positioned within the aperture alongside

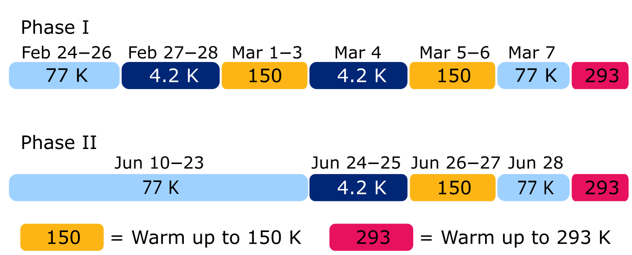


FIG. 11. Timeline of the two-phase cold tests in 2025.

energy loss measurements at 77 and 4.2 K. The peak operational current during the Phase I campaign reached 5.750 kA.

Following the warm-up to room temperature, the Stycast volume within the magnet bore was mechanically extracted, and an anticryostat was inserted into the cleared aperture to facilitate the field-quality measurement during Phase II.

Phase II testing started with a 77 K validation run to verify the magnet condition after the thermal cycle and Stycast removal. During the subsequent 4.2 K test, the magnet reached a peak current of 6.795 kA.

Magnetic-field harmonics were measured using a high-precision rotating coil probe developed by FNAL [95]. The probe assembly incorporates five independent, 100-mm-long induction circuits aligned along its longitudinal axis. In addition to the field at the magnet center, spatial profile mapping was conducted by stepping the probe along the bore axis. The nominal rotation speed of the probe was 2 to 3 Hz. The harmonic measurement resolution is between 0.01 and 0.001 units at a reference radius of 22.5 mm, matching the outermost measurement trace geometry of the rotating probe.

Data-acquisition configurations varied by operational temperature. For room temperature and 77 K tests, voltage signals from the individual layers, the whole magnet, and the cryogenic Hall probe were routed directly to National Instruments NI-9238 data acquisition cards. The current transducer signal was captured concurrently via an NI-9239 card. The system sampling rate was between 1.6 and 2.0 kHz.

At 4.2 K, voltage signals from the individual layers and the magnet were isolated and amplified using Advantech ADAM-3014 modules, in addition to a customized isolation-amplifier assembly.

Active quench detection during the 4.2 K tests was implemented via dual-track redundancy: an in-house developed Field Programmable Gate Array, FPGA, framework operating in parallel with an NI FlexLogger system. Above a certain operational current threshold, the quench trigger condition was defined by a resistive voltage exceeding 250 μV sustained over a validation time window of 100 to 200 ms. Upon a trigger event, a digital signal would be instantly routed to the power supply controller and active quench protection infrastructure. The active protection scheme would execute energy extraction by connecting the magnet circuit across a 20 mΩ resistor.

Distributed fiber-optic sensing networks were integrated into all six conductor layers and on the aluminum shell, building upon the baselines established in Ref. [96]. Detailed results will be reported elsewhere. Real-time temperature monitoring of the magnet shell was also provided by two calibrated Cernox® temperature sensors affixed to the upper and lower longitudinal margins of the outer aluminum shell. Continuous voltage tracking was maintained during cooldown and warm-up via a 100-mA low-current excitation of the magnet.

## VI. PERFORMANCE OF THE WITNESS SAMPLES

To establish a representative performance baseline for each layer, 1-m-long witness samples were harvested from the end of the respective CORC® wire spools after winding each C3 magnet layer. The critical current of these six witness samples was evaluated at 4.2 K by ACT. It is assumed that the performance of the witness sample represents the performance of the entire wire piece for each layer.

Each sample was bent into a U-shape with a nominal radius of 31.5 mm and tested in the aperture of a superconducting solenoid magnet. The background magnetic induction vector aligned parallel to the straight vertical legs of the sample assembly. Complete details on the sample configuration and measurement setup are reported in Ref. [62].

Figure 12 shows the voltage-current, $V(I)$, characteristics measured from Layer 6 witness sample as a function of both transport current and applied magnetic induction.

The measured $V(I)$ data were fitted to the following power-law relation to determine the critical current $I_c$ at each applied magnetic induction,

$$V = V_{\text{offset}} + IR + V_c \left(\frac{I}{I_c}\right)^n, \tag{1}$$

where $V_{\text{offset}}$ represents the voltage offset and $R$ is the joint contact resistance resolved across the voltage taps. The critical current is defined at a voltage criterion, $V_c$, of 5 μV. Since some of the maximum voltage measured across the witness samples and magnet layers were around 5 μV or lower, this conservative criterion was selected to minimize the extrapolation and associated uncertainty and to suppress uncertainties when comparing the performance

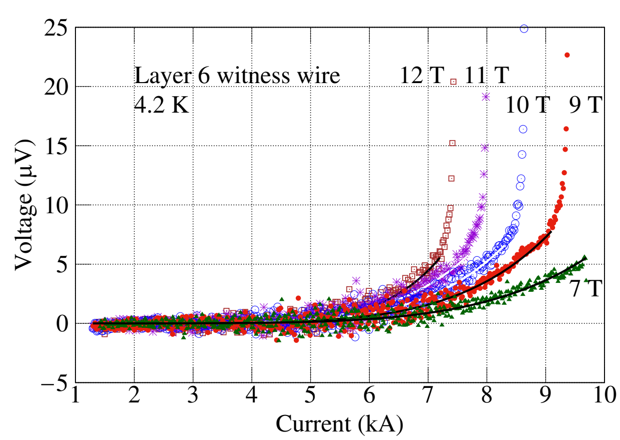


FIG. 12. The voltage across Layer 6 witness wire as a function of current and applied magnetic induction at 4.2 K. Solid lines are the fit up to 8 μV according to Eq. (1).

TABLE III. The measured critical current, $n$ value and the corresponding overall wire current density, $J_{\mathrm{overall}}$, and $\vec{I} \times \vec{B}$ force on the Layer 6 witness sample at its critical current at 4.2 K. Voltage criterion: 5 μV.

| $B_{\mathrm{app}}$ (T) | 12 | 11 | 10 | 9 | 7 |
|---|---|---|---|---|---|
| $I_c$ (kA) | 7.104 | 7.509 | 7.944 | 8.460 | 9.517 |
| $J_{\mathrm{overall}}$ (A mm$^{-2}$) | 626 | 662 | 700 | 746 | 839 |
| $n$ (–) | 7.7 | 6.2 | 6.3 | 6.1 | 5.7 |
| Force (kN m$^{-1}$) | 85 | 83 | 79 | 76 | 67 |

between the witness samples and magnet layers and between the magnet layers.

Table III compiles the resulting critical current and $n$ value for the Layer 6 witness sample at 4.2 K. The derived overall wire current density and corresponding transverse $\vec{I} \times \vec{B}$ force on the sample at its critical current are also included.

Figure 13 shows the electromagnetic $\vec{I} \times \vec{B}$ force profiles on each witness sample at 4.2 K. The peak force reached 90 kN m$^{-1}$ for the witness samples of Layers 1 and 2.

The field-dependent scaling of the wire critical current within 6 to 12 T is modeled linearly on a double-logarithmic scale [62], following

$$\log\left(\frac{I_c}{1\ \mathrm{A}}\right) = \alpha \log\left(\frac{B}{1\ \mathrm{T}}\right) + c, \tag{2}$$

where $\alpha$ and $c$ represent the scaling slope and intercept parameters, respectively. The constant of 1 A and 1 T in Eq. (2) makes the argument of the logarithm dimensionless.

Table IV gives the fitted parameters compiled across all six witness samples. The high statistical convergence is verified by the reported coefficients of determination, $R^2$,

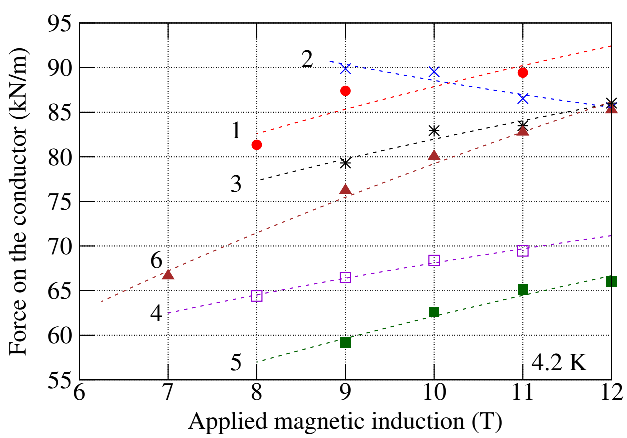


FIG. 13. Electromagnetic $\vec{I} \times \vec{B}$ force sustained by individual layer witness samples at 4.2 K as a function of applied magnetic induction. Dashed lines indicate the calculation based on the fitting parameters from Table IV.

TABLE IV. Double-logarithmic scaling parameters $\alpha$ and $c$ for the $I_c(B)$ at 4.2 K across the six layer-specific witness samples.

| Layer | 1 | 2 | 3 | 4 | 5 | 6 |
|---|---|---|---|---|---|---|
| $\alpha$ | −0.72 | −1.19 | −0.74 | −0.76 | −0.61 | −0.54 |
| $c$ | 4.67 | 5.14 | 4.65 | 4.59 | 4.41 | 4.44 |
| $R^2$ | 0.97 | 1.00 | 0.99 | 1.00 | 0.98 | 0.99 |
| Range (T) | 8–11 | 9–12 | 9–12 | 8–11 | 9–12 | 7–12 |

alongside the explicit magnetic-field intervals used to bound each regression. We used the empirical model to determine the expected magnet performance in Sec. III.

## VII. CURRENT-CARRYING CAPABILITY OF THE MAGNET

### A. 77 K tests

Figure 14 shows the voltage across each layer measured during the cooldown from room temperature to 77 K.

Figure 15 shows the layer voltage as a function of current at 77 K. Before the assembly, each layer was tested individually, whereas after assembly, the layers were mechanically nested and electrically connected in series. Therefore, the after-assembly test terminated at the same current value for all the layers. The measurement stopped at 210 A to limit the peak voltage across Layer 1. The voltage offset and voltage due to the termination resistance were removed according to Eq. (1).

Table V summarizes the pre- and postassembly critical currents and $n$ values for each layer, alongside the postassembly critical-current retention compared to the post-Stycast baseline. Data for Layers 3–5 are omitted because their voltage responses did not reach the 1 μV threshold at the 210 A peak current (Fig. 15). For Layers 2 and 6, low-voltage development required us to extrapolate the $V(I)$ fitting to determine the critical currents.

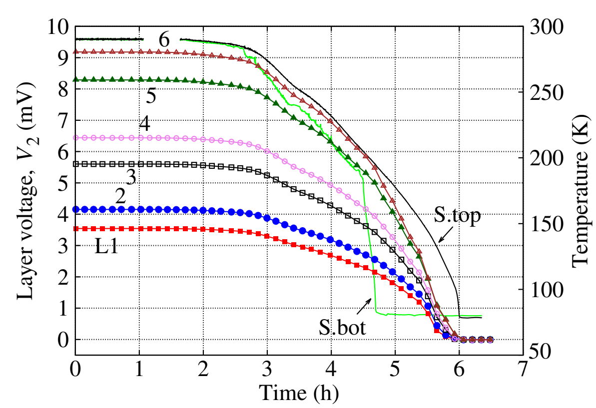


FIG. 14. Voltage across each layer of the C3 magnet at 100 mA during the cooldown from room temperature to 77 K. Secondary $y$ axis: Readings of the temperature sensors attached to the top (S.top) and bottom (S.bot) edges of the aluminum shell.

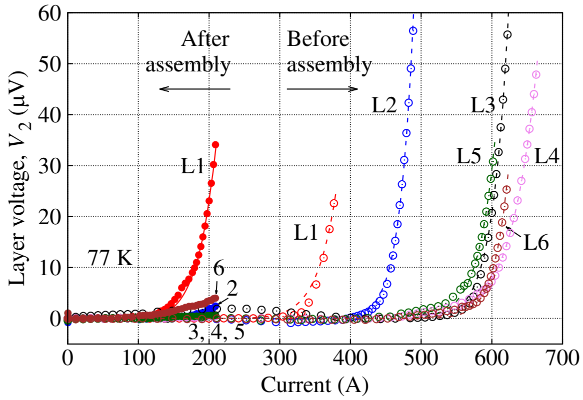


FIG. 15. Voltage across each layer of the C3 magnet before and after magnet assembly. 77 K. Open symbols and dashed lines: Voltage of an individual layer measured before the assembly. Solid symbols and lines: Voltage of an individual layer after the assembly.

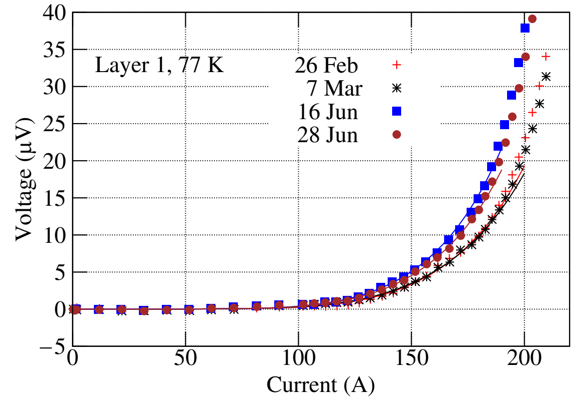


FIG. 16. Voltage across Layer 1 before and after the first 4.2 K test (February 27–March 4) and second 4.2 K test (June 24–June 25). 77 K, self-field. Solid lines are exponential fits according to Eq. (1).

Figure 16 compares the 77 K $V(I)$ curves for Layer 1 before and after the 4.2 K tests. After warming to room temperature between March 7 and June 16 (Fig. 11), Layer 1 experienced a 6.3% reduction in critical current (160 A down to 150 A) and a slight increase in $n$ value (5.8 to 6.2). No significant changes were observed in the $V(I)$ behavior for the other layers.

### B. 4.2 K tests

Figure 17 shows the preset and actual peak current during the 4.2 K tests. The magnet current was ramped down to zero at a rate of 25 $\mathrm{A\,s^{-1}}$ upon reaching the preset target level after holding for 30 s. We gradually increased the target peak current for the following ramp, based on the layer voltage from the previous ramp. The peak current did not increase monotonically with each sequential ramp because of the tests at low currents and a few false alarms from the quench detection scheme. The C3 magnet did not quench or thermally run away during the tests. Figure 17 also shows the peak $\vec{I} \times \vec{B}$ force on the CORC® wire at different periods of the 4.2 K test.

Strong inductive voltage was observed across each layer during ramping. The inductive component decayed and the resistive component remained when the current ramping paused for about 30 s. Figure 18 shows an example of the voltage profiles measured with a stepwise current profile with intermediate current-holding plateaus. We averaged the raw voltage data over the last 3 s at each current plateau during the up-ramp to determine the resistive voltage across each layer (Fig. 18).

Layer 1 had the highest resistive voltage of 105 μV at 6.795 kA, followed by Layer 4 of 20 μV (Fig. 19). The current is about 70% along the load line for Layer 1 (Table VI). The remaining layers had a maximum voltage less than 6 μV (Fig. 20).

Table VI compiles the critical current and $n$ value for each layer as determined according to Eq. (1). Compared to Layers 1, 4, and 5, the values for Layers 2, 3, and 6 have a larger uncertainty because their resistive voltages were lower than 5 μV at the maximum current.

TABLE V. The critical currents and $n$ values of individual layers before and after application of Stycast and after magnet assembly. 77 K, self-field. Voltage criterion: 5 μV.

| | Before Stycast | | After Stycast | | After assembly[a] | | |
|---|---|---|---|---|---|---|---|
| | $I_c$ | $n$ | $I_c$ | $n$ | $I_c$ | $n$ | $I_c$ retention |
| Layer | (A) | (–) | (A) | (–) | (A) | (–) | (–) |
| 1 | 353 | 21.3 | 348 | 20.9 | 160 | 5.8 | 46% |
| 2 | [⋯] | [⋯] | 447 | 30.3 | ~239 | ~7.3 | ~53% |
| 3 | [⋯] | [⋯] | 575 | 35.1 | >210 | [⋯] | >37% |
| 4 | [⋯] | [⋯] | 581 | 14.7 | >210 | [⋯] | >36% |
| 5 | [⋯] | [⋯] | 550 | 14.7 | >210 | [⋯] | >38% |
| 6 | [⋯] | [⋯] | 587 | 26.8 | ~243 | ~3.5 | ~41% |

[a]Measured on February 24–26 before the first 4.2 K test (Fig. 11).

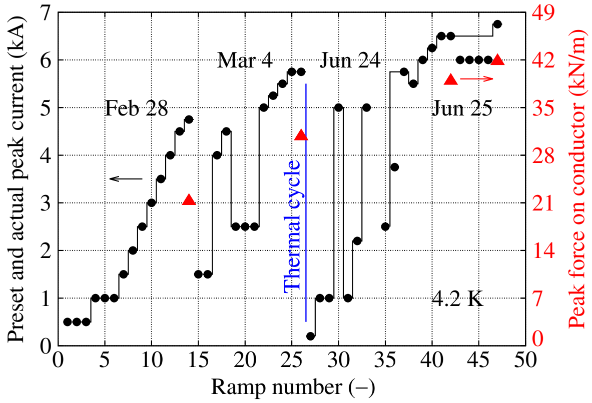


FIG. 17. Primary $y$ axis: The preset peak current for each ramp in solid lines and the actual peak current in closed circles. Secondary $y$ axis: The peak $\vec{I} \times \vec{B}$ force on the conductor in red triangles. The blue vertical line in the center represents the thermal cycle between March 4 and June 24.

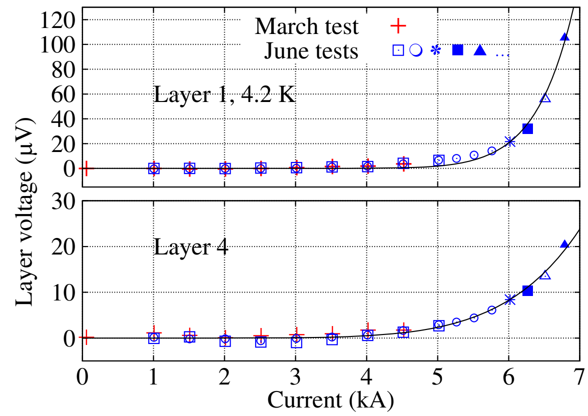


FIG. 19. Resistive voltage across Layers 1 and 4 as a function of current at 4.2 K. The solid lines are the fit according to Eq. (1).

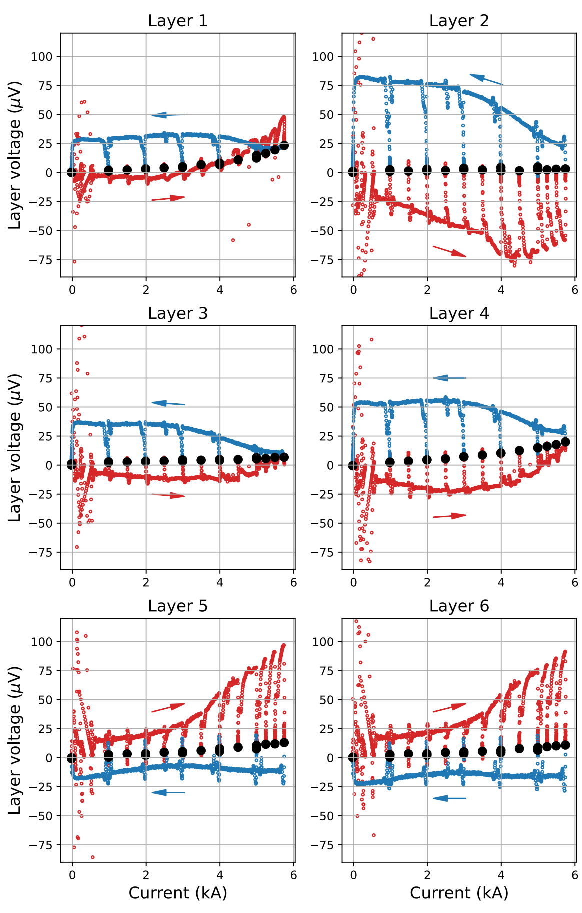


FIG. 18. Voltage across each layer as a function of current up to 5.750 kA at 4.2 K. The red points denote the raw voltage during the up-ramp of the current and the blue points during the down-ramp. The black points are the resistive voltage during the up-ramp. The arrows indicate the up- and down-ramp branches of the current.

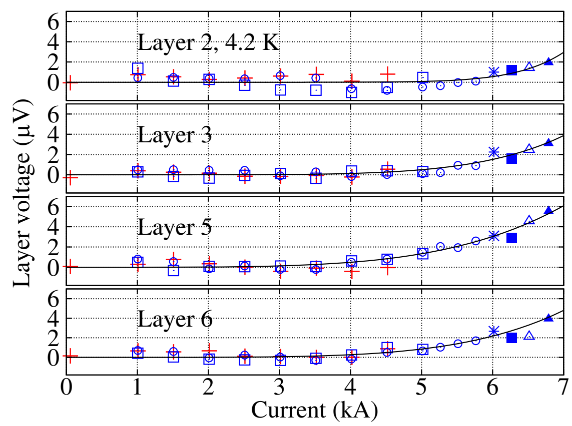


FIG. 20. Resistive voltage across Layers 2, 3, 5, and 6 as a function of current at 4.2 K. The legends are identical to those in Fig. 19. The solid lines are the fit according to Eq. (1).

TABLE VI. The critical current and $n$ value of each layer at 4.2 K from the June test. SSP stands for the short-sample prediction for each layer. The last column is the ratio between the critical current at 4.2 and 77 K. Voltage criterion: 5 μV.

| | $I_c$ (4.2 K) | $n$ (4.2 K) | SSP | $I_c$/SSP | $\times I_c$(77 K) |
|---|---|---|---|---|---|
| Layer | (kA) | (–) | (kA) | (–) | (–) |
| 1 | 4.772 | 5.2[a] | 9.768 | 49% | 30 |
| 2 | ~7.347 | ~10.9 | 10.146 | ~72% | 31 |
| 3 | ~7.300 | ~6.1 | 9.652 | ~76% | <35 |
| 4 | 5.580 | 6.9 | 8.911 | 63% | <27 |
| 5 | 6.702 | 4.5 | 8.475 | 79% | <32 |
| 6 | ~7.054 | ~5.2 | 10.214 | ~69% | 29 |

[a]The $n$ value was determined by fitting the $V(I)$ data up to 20 μV.

## VIII. FIELD QUALITY

The magnetic field in the transverse $x$-$y$ plane of the aperture is given by

$$B_y + iB_x = B_1 \times 10^{-4} \sum_{n=1}^{\infty} (b_n + i a_n) \left( \frac{x + iy}{R_{\mathrm{ref}}} \right)^{n-1}, \quad (3)$$

where the $z$ axis aligns with the magnet's longitudinal axis [97]. $b_n$ is the normal and $a_n$ is the skew multipolar coefficient of the order $n$. The coefficients are normalized to the main dipole field, $B_1$, and expressed in units of $10^{-4}$ at a reference radius of 22.5 mm. The radius covers about 55% of the aperture as determined by the position of the Layer 1 wire or 69% of the clear aperture (Table II). The harmonics reported here are uncorrected for centering. We define the dipole transfer function, $T_1$, as the ratio of the dipole field to the magnet current, expressed in $\mathrm{T\,kA^{-1}}$.

### A. Field profiles along the magnet aperture

Figure 21 shows the longitudinal $T_1$ profile measured at 286, 77, and 4.2 K under constant current. The corresponding field calculations reflect the nominal coil geometry and include iron yoke saturation but omit magnetization effects in the CORC® wires.

Figure 22 plots the longitudinal profile of $b_3$ measured along the magnet aperture at different temperatures. The solid line gives the calculated profile considering only the geometric and iron effects. The center part of the calculated profile, between $z = \pm 70$ mm, was shifted by −49 units to match the 77 K measurement and by −28 units to match the 4.2 K measurement.

### B. Field profiles during current ramping

Figure 23 shows the dipole transfer function, $T_1$, measured at the magnetic center from five current ramps at 4.2 K. Ramp 40 attained a peak current of 6.266 kA. For Ramps 44–46, the power supply aborted at 5.966 kA due to false alarms from the voltage-detection scheme. During Ramp 47, the magnet reached the preset current of 6.795 kA, generating a dipole field of 5.99 T. Following a 28 s flattop hold at this current, the power supply tripped. The cause is unknown. It was not a magnet quench because the resistive voltage was stable across the layers when the power supply tripped.

The reproducibility of the dipole transfer function was evaluated using the profiles from Ramps 44–47. Figure 24 shows the relative standard deviation, defined as the ratio between the standard deviation of $T_1$ and the mean value of $T_1$ across the four measurements. The field-dependent reproducibility reached 0.01% as the dipole field reached 5 T.

Figure 25 shows the field-dependent normal $b_n$ and skew $a_n$ magnetic-field harmonics up to the dodecapole, measured from Ramp 40 (Fig. 17).

Table VII gives the normal and skew harmonics measured at a dipole field of 5.99 T.

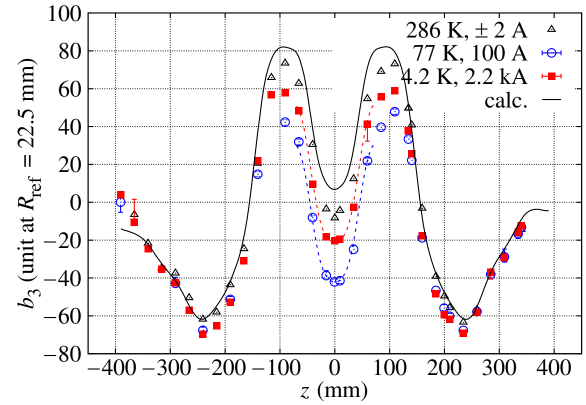


FIG. 22. $b_3$ along the magnet aperture. The dashed lines are the center part of the calculated profile, between $z = \pm 70$ mm, shifted to match the measurements, as a visual guide.

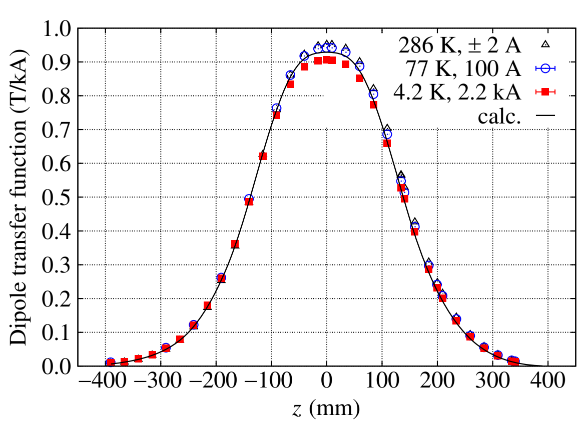


FIG. 21. $T_1$ along the magnet aperture in $z$ direction. The solid line is the calculated value.

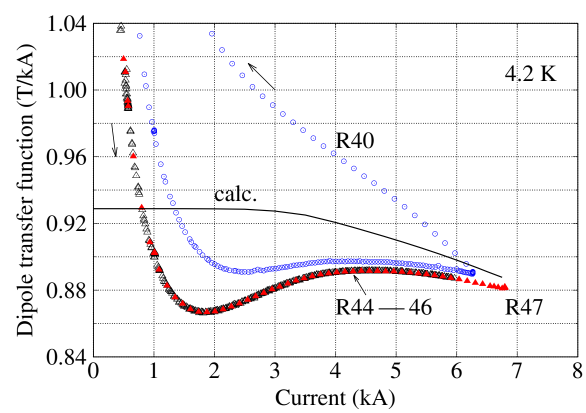


FIG. 23. The measured dipole transfer function at 4.2 K from Ramps 40 and 44–47. The ramp number is defined in Fig. 17. The black solid line is the calculated value. The arrows indicate the up- and down-ramp branches.

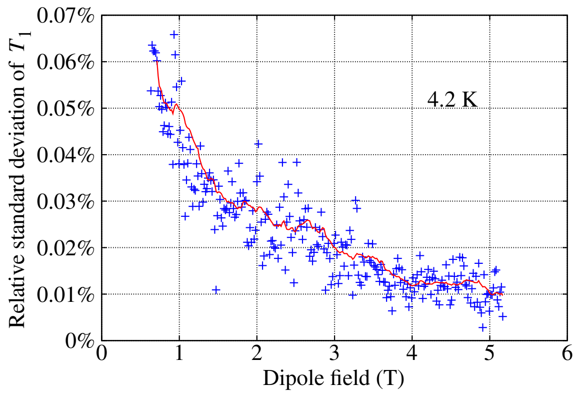


FIG. 24. The relative standard deviation of $T_1$ from the last four ramps, R44–R47, as shown in Fig. 23. The red line is the 20-point moving average.

TABLE VII. Harmonics at a dipole field of 5.99 T and 6.795 kA at 4.2 K. $R_{\mathrm{ref}} = 22.5$ mm.

| $n$ | 2 | 3 | 4 | 5 | 6 | 7 | 8 | 9 |
|---|---|---|---|---|---|---|---|---|
| $b_n$ | 1.9 | −24.7 | 0.3 | −3.3 | −0.1 | −0.3 | −0.0 | −0.0 |
| $a_n$ | 2.4 | −1.0 | 0.2 | −0.3 | −0.0 | 0.0 | −0.0 | 0.0 |

The magnet was not conditioned to a reproducible magnetization state prior to the measurement. The prior ramp, Ramp 36, aborted at 3.750 kA during the up-ramp due to a false detection (Fig. 17).

Figure 27 shows the measured decay of the $b_3$ when the magnet current was held at 3.510 kA. Ignoring the current oscillation between 325 and 329 s, we fit the remaining decay profile using an exponential function [98]:

$$\Delta(d, t, \tau) = d_0 + d\left[1 - \exp\left(\frac{t_0 - t}{\tau}\right)\right], \quad (4)$$

where $t_0$ represents the decay initiation time, $d_0$ is the initial amplitude of $b_3$ at $t_0$, $d$ is the asymptotic decay amplitude, and $\tau$ the characteristic decay time constant.

Table VIII compiles the extracted regression parameters governing the $b_3$ decay across different current levels during the up-ramp up to 5.759 kA and the following down-ramp.

### C. Decay and snapback of $b_3$

Dynamic field decay and subsequent snapback were observed at 77 and 4.2 K across multiple allowed field harmonics, including the main dipole field $T_1$ and the sextupole component $b_3$. These phenomena were measured using a stepwise current profile. Figure 26 shows an example from $b_3$, measured at various current plateaus. The ramp rate was 25 A s$^{-1}$ between the current plateaus. Each plateau was set to last for 30 s.

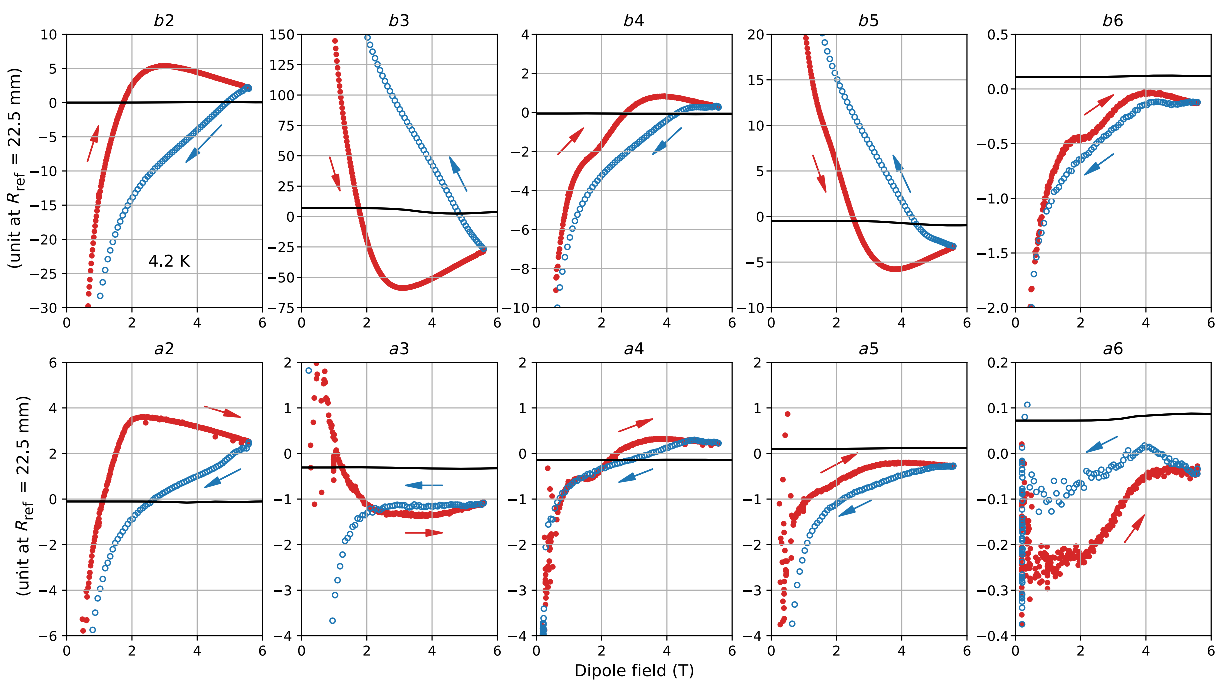


FIG. 25. Harmonics measured at 4.2 K as a function of dipole field at $R_{\mathrm{ref}} = 22.5$ mm during Ramp 40. No centering correction was applied. Top row: $b_2$-$b_6$. Bottom row: $a_2$-$a_6$. Red solid circles: up-ramp. Blue open circles: down-ramp. The arrows indicate the up- and down-ramp branches. The black lines are the calculated harmonics without considering the magnetization effect.

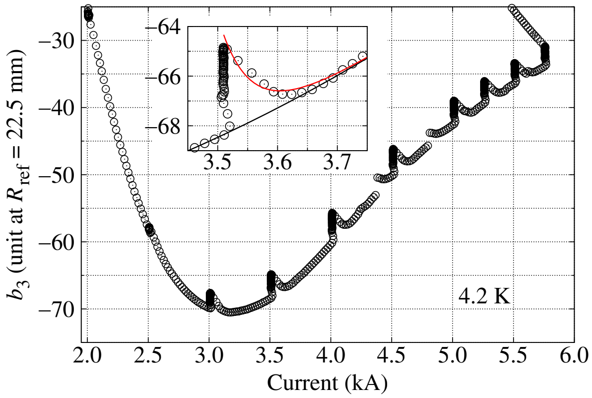


FIG. 26. Measured decay and snapback profile of $b_3$ at various current levels and 4.2 K. The inset shows the behavior when the current was held at 3.510 kA. The black line is a fit to the $b_3$ data without the current plateau. The red solid line is an exponential fit of the snapback part according to Eq. (5).

The snapback of $b_3$ as a function of current was also fitted with an exponential function [98],

$$b_{3,\mathrm{snapback}} = d \exp\left(\frac{I_0 - I}{\Delta I}\right), \tag{5}$$

where $I_0$ is the amplitude of the current plateau, $I$ is the current following the plateau, and $d$ and $\Delta I$ represent scaling fitting parameters. $b_{3,\mathrm{snapback}}$ is the difference between the measured $b_3$ and baseline $b_3$ without the current plateau.

The inset in Fig. 26 gives an example of the exponential fit of the snapback with $d = 4.0$ unit and $\Delta I = 0.051$ kA and $I_0 = 3.510$ kA.

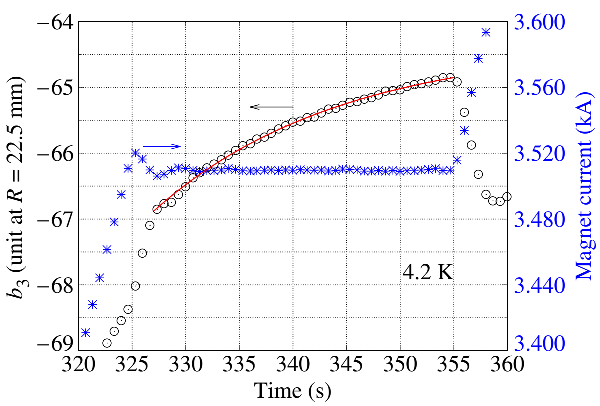


FIG. 27. Primary $y$ axis: Time-resolved decay of $b_3$ when the magnet current was held around 3.510 kA at 4.2 K. The solid red line denotes the exponential fit of the $b_3$ according to Eq. (4). Secondary $y$ axis: Synchronous magnet current as a function of time.

TABLE VIII. Extracted fitting parameters of the $b_3$ decay at different current levels at 4.2 K according to Eq. (4). The upper section is for the up-ramp and the lower section for the down-ramp. $B_1$ is the measured dipole field at each current level. $R_{\rm ref} = 22.5$ mm. RMSE denotes the root-mean-square error of the regression.

| $I$ | $B_1$ | $d_0$ | $t_0$ | $d$ | $\tau$ | RMSE |
|---|---|---|---|---|---|---|
| (kA) | (T) | (unit) | (s) | (unit) | (s) | (unit) |
| 1.005 | 0.96 | 113.0 | 80 | −0.1 | 1.2 | 0.038 |
| 2.007 | 1.78 | −26.0 | 180 | −0.5 | 18.6 | 0.024 |
| 2.508 | 2.23 | −58.1 | 230 | 0.3 | 16.3 | 0.013 |
| 3.010 | 2.68 | −68.7 | 279 | 1.4 | 16.8 | 0.018 |
| 3.510 | 3.14 | −66.6 | 329 | 2.3 | 17.3 | 0.021 |
| 4.011 | 3.60 | −58.4 | 377 | 3.3 | 17.3 | 0.026 |
| 5.012 | 4.50 | −41.0 | 478 | 2.5 | 17.3 | 0.021 |
| 5.759 | 5.15 | −32.3 | 601 | 1.8 | 19.3 | 0.013 |
| 5.009 | 4.62 | −11.7 | 662 | 0.1 | 17.8 | 0.010 |
| 3.007 | 2.95 | 77.6 | 801 | −1.3 | 15.1 | 0.028 |
| 1.005 | 1.13 | 263.7 | 941 | −5.8 | 17.0 | 0.148 |

## IX. ENERGY LOSSES

The energy loss of the magnet per operational cycle is defined as the net differential between the electromagnetic energy absorbed during charging and that recovered during discharging. Following the methods detailed in Refs. [99,100], we measured the energy loss of the C3 magnet using trapezoidal current profiles bounded between 10 and 100 A at 77 K and between 1.0 and 2.5 kA at 4.2 K. The current range was selected to reduce the resistive voltage component.

Three cycles were measured for the same current ramp rate. We report the loss data averaged from three cycles. Figure 28 gives an example of the measured current and

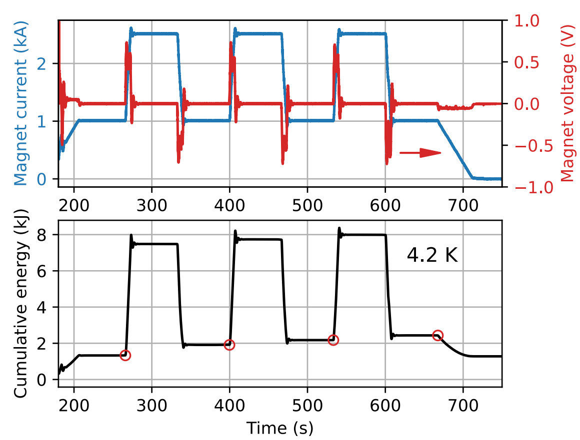


FIG. 28. Top: The magnet current on the primary $y$ axis and the voltage across the magnet on the secondary $y$ axis, during the cycles at 4.2 K. Bottom: The cumulative energy as a function of time. The difference between the two neighboring energy levels marked by the red circles is the energy loss of one cycle.

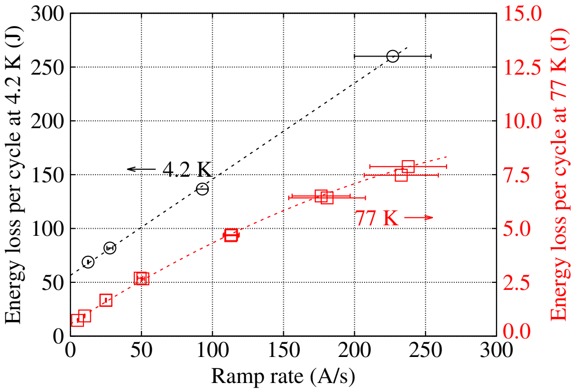


FIG. 29. Measured energy loss per cycle of the C3 magnet at 4.2 K, black circles on the primary $y$ axis, and at 77 K, red squares on the secondary $y$ axis. The dashed lines are the fit. The $x$ error bars indicate the ±3 standard deviation of the measured ramp rates.

voltage profile at 4.2 K with a nominal current ramp rate of 226 A $s^{-1}$ between 1.0 and 2.5 kA.

Figure 29 shows the total energy loss per cycle measured at 77 and 4.2 K as a function of the current ramp rate.

The rate-dependent energy losses are parameterized by

$$E_1 = 0.89\, r + 56.47, \tag{6a}$$

$$E_2 = -5.05 \times 10^{-5}\, r^2 + 4.27 \times 10^{-2}\, r + 0.56, \tag{6b}$$

where $E_1$ in J per cycle is a linear fit of the 4.2 K data, $E_2$ is a quadratic fit of the 77 K data, and $r$ is the ramp rate of the current in A $s^{-1}$. Ignoring the contribution from the iron magnetization and the current oscillation at the end of each up-ramp, the zero-rate intercept in Eq. (6) provides a measure of the hysteresis loss per cycle in the CORC® wires.

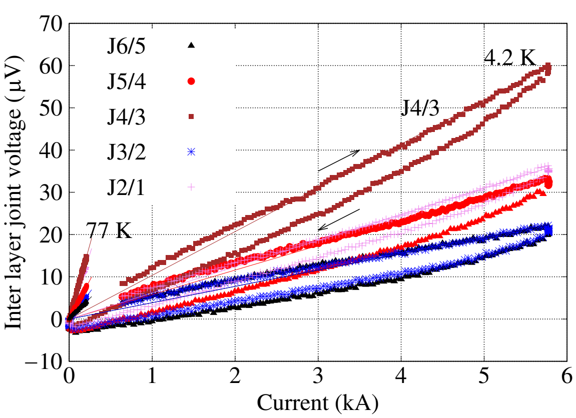


FIG. 30. Voltage across the interlayer joints of the C3 magnet as a function of current at 77 and 4.2 K. The solid lines are the linear fit of the up-ramp branch of the measured data. The arrows indicate the up- and down-ramp branches of the voltage at 4.2 K.

TABLE IX. Measured resistance across the interlayer joints. An averaged ratio between the resistances at 77 and 4.2 K is also given for each joint.

| | Feb. Mar. tests | | June test | | |
|---|---|---|---|---|---|
| | 77 K | 4.2 K | 77 K | 4.2 K | |
| Joint | (nΩ) | (nΩ) | (nΩ) | (nΩ) | Ratio(–) |
| 6/5 | 20 | 3.9 | 20 | 3.4 | 5.5 |
| 5/4 | 37 | 5.8 | 38 | 5.4 | 6.7 |
| 4/3 | 71 | 10.4 | 72 | 9.3 | 7.3 |
| 3/2 | 26 | 3.9 | 26 | 3.3 | 7.3 |
| 2/1 | 62 | 6.2 | 64 | 5.8 | 10.5 |

## X. ELECTRICAL TERMINATIONS

Figure 30 gives the measured voltage across each interlayer joint as a function of current at 77 and 4.2 K. We report the slope of the up-ramp of the voltage profile as the resistance across the interlayer joint, as shown in Table IX.

## XI. DISCUSSION

### A. Magnet fabrication

The fabrication of the C3 layers consisted of three main steps: coil winding, Stycast impregnation, and a preliminary qualification test at 77 K before assembly. No high-temperature bake was needed after winding because the conductor is already superconducting. This is a blessing and a curse; more on this point in Sec. XI D.

The layer fabrication and assembly process for the C3 magnet showed that the round CORC® wires worked well with the CCT design. One highlight was the winding of all the layers using a prototype winding machine. We consider automated coil winding important for scaling the REBCO magnet technology [101–103]. It enforces a deterministic winding process across multiple coils and minimizes manual handling variations. It can reduce the cost of coil winding when it matters. The successful winding of six layers demonstrates a useful step toward fully automated and reproducible winding of CCT coils using round REBCO conductors.

The painting and curing of the Stycast consumed 30%–50% of the total fabrication time per layer (Fig. 7). It was driven by a two-stage application protocol: an initial pass encapsulated the coil winding and anchored the lead wire held in place by rubber pieces, followed by a second remediation pass to fill the voids after removing the rubber pieces and the minor cavities postcure. We need an automated procedure to impregnate long coils. A low-viscosity vacuum pressure impregnation process using room-temperature curing medium offers a viable path for future magnets [104].

The structural integration provided by the inter- and intralayer Stycast matrix effectively immobilized the

CORC® wire against peak electromagnetic force up to 42 kN m$^{-1}$ at 4.2 K. This is confirmed by the absence of micromovement-induced voltage transients during the current ramping (Fig. 18). Conversely, the previous C2 magnet had less Stycast impregnation, resulting in frequent voltage spikes indicative of conductor displacement, despite sustaining less than half the peak electromagnetic force of the C3 magnet [61].

The alumina-filled Stycast also improved the thermal conduction between the layers. This enhanced thermal coupling led to a highly uniform cooldown profile, with all six layers transitioning together, as shown by the voltage decrease during the cooldown (Fig. 14). A similar behavior was also observed in the C3a magnet, where the layer gaps were filled with Stycast [63]. In contrast, the previous C2 magnet lacking interlayer thermal fillers exhibits a sequential superconducting transition from the outer to the inner layers [61].

Gluing all the layers with Stycast has a drawback. It prevents nondestructive disassembly or selective replacement of a layer when needed. For instance, replacing Layers 1 and 4 in the C3 magnet can lead to a higher dipole field. Using shims to mechanically couple all the layers is a proven solution [85,105].

The electrical termination and joints worked as expected. Similar to the C3a magnet, the interlayer joint between Layers 3 and 4 consistently showed the highest resistance [63]. This was likely caused by the geometric tolerances in the reusable Cu adapters shared by both magnets.

The hysteresis behavior of the voltage across the termination indicates that the current sharing with the superconducting tapes inside the termination may affect the measured voltage. A cryogenic calorimetric method is required to measure the total volumetric heat generation of the electrical joint for CORC® wires.

## B. Magnet behavior

### 1. *High thermal stability and reproducible resistive voltage across layers*

The C3 magnet showed reproducible layer-voltage profiles across current ramps at 4.2 K. The stable voltage profile over multiple current ramps was also observed in other HTS magnets [40,83].

Measurable resistive voltage started occurring in several layers when the current reached approximately 4 kA, corresponding to a dipole field of 3.5 T (Figs. 19 and 20). During the operations exceeding 4 kA (Fig. 17), the peak Joule dissipation within Layer 1 was calculated at 0.7 W during the current plateau. No thermal runaway of the magnet occurred at the end of the current holding, highlighting the thermal stability of the C3 magnet, consistent with the observations in other REBCO magnets [40,43]. To minimize steady-state Joule dissipation at the target dipole field, future REBCO magnets must incorporate enough performance or current margin relative to the nominal operating envelope.

Four consecutive current ramps were consistently limited at 6 kA (Fig. 17) due to a wrong setting in the voltage-detection scheme implemented in the FlexLogger program. Although unintended, this systematic interruption demonstrated the reproducibility of the voltage signals and their efficacy for active protection of the short experimental REBCO magnets. However, the scalability of the voltage-based method for long-length REBCO magnets remains unverified. Alternative detection methods need to be developed [106,107].

Furthermore, the integrated layer-voltage monitoring lacks the spatial resolution required to isolate the precise distribution of resistive and thermal dissipation along the CORC® wire. Since the voltage taps were embedded within the electrical terminations, a non-negligible fraction of the measured resistive voltage drop may originate within the terminations rather than the coils. Identifying the exact spatial distribution of local heat sources is therefore critical to understanding and addressing the factors that limit the magnet performance [108–110].

The electromagnetic force up to 42 kN m$^{-1}$ induced no measurable degradation in the CORC® wires, as verified by the reproducible $V(I)$ data of Layer 1 before and after the 4.2 K test (Fig. 16). This is expected because the peak electromagnetic load was about half of the $\vec{I} \times \vec{B}$ force sustained during the witness-sample test, which exhibited no obvious sample degradation (Fig. 13). Furthermore, the peak force was only 37% of the 115 kN m$^{-1}$ degradation threshold established for the nonimpregnated, bare CORC® wire under direct transverse compression [111]. A CORC® wire impregnated by Stycast can sustain a higher transverse compression up to 600 kN m$^{-1}$ [112].

### 2. *Strong magnetization effect in field quality*

At a dipole field of 5 T, the transfer function of the dipole field satisfied the minimum repeatability of 0.01% for accelerator magnet applications (Fig. 24) [113]. We suspect that as the field on the conductor increased, the magnetization in the CORC® wire decreased and helped improve the reproducibility of the dipole field.

The dipole field and high-order terms, $b_3$ and $b_5$, showed strong hysteresis (Figs. 23 and 25). The hysteresis width of the dipole field is approximately one order of magnitude higher than that of a REBCO dipole magnet using the aligned-block design [114].

The magnetization effect also induced a deviation of the $b_3$ from its geometric value within the center region of the magnet (Fig. 22). A similar behavior was observed in a $\cos\theta$ dipole magnet wound using a single REBCO tape [115]. The attenuated $b_3$ profile shift at 4.2 K relative to 77 K did not stem from a lower critical-current density; rather, it was because of the magnetization-induced $b_3$

tracking through a near-zero crossover point at 2.2 kA, or 2 T dipole field, at 4.2 K (Fig. 25).

The strong hysteresis was largely due to the magnetization effect that scales with the effective superconducting filament width [116]. In the C3 magnet, the perpendicular component of the changing magnetic field relative to the longitudinal axis of the CORC® wire imposed an effective filament size on the order of mm, matching the full physical width of the embedded tapes [117]. Conversely, the REBCO tapes within the aligned-block configuration are largely aligned with the local magnetic flux lines [39], bounding the effective filament size to the μm-scale thickness of the superconducting REBCO layer itself.

The magnetization also scales with the conductor critical-current density [116]. As the magnetic field increased, the critical-current density in REBCO conductors decreased, so did the hysteresis in the main field and harmonics (Fig. 25).

Aligning REBCO tapes with local magnetic flux lines introduces a trade-off. At 4.2 K, the critical current of a REBCO tape peaks when the broad surface is oriented parallel to the applied magnetic field. The higher critical current can increase the magnetization-induced field errors despite the geometric reduction in the effective filament size [118].

The large magnetization effect in the field quality can be mitigated by reducing the width of the REBCO layer via laser striation [119] or by using passive ferromagnetic shims [25,120]. Furthermore, the conductor path within the CCT design can be parametrically tuned to compensate for the magnetization-induced field errors at a target dipole field [72]. Depressing the critical-current density in REBCO conductors is not appealing for high-field accelerator magnets because a high critical-current density is necessary to reduce conductor usage and minimize total coil cross section.

#### *3. Higher hysteresis loss than the SSC Nb-Ti model dipole magnet*

Minimizing the energy loss during current ramping can reduce the undesired heat load to the magnet and cryogenic system. The hysteresis loss, contributing to the total volumetric dissipation, is a concern for REBCO conductors because of its large filament size, high critical-current density, and potentially a large field swing during the operation of a high-field REBCO magnet.

In Table X, we contrast the measured energy loss per cycle between the C3 magnet and the short model Nb-Ti dipole magnets developed for the Superconducting Super Collider (SSC) [99]. Both have a comparable coil width of approximately 24 mm [121]. The loss data are normalized to the magnetic length of the magnet: 0.3 m for the C3 magnet (Fig. 21) and 1.5 m for the SSC model magnet.

Although the two magnets differ in the design, size, and magnetic-field bounds for the measurement, all affecting the energy loss, the comparison underscores the significant difference in the hysteresis loss. Specifically, the hysteresis loss per unit magnetic length of the C3 magnet almost triples that of the SSC model magnet, despite being evaluated over a narrower dipole field range. The hysteresis loss in the C3 magnet will further increase if the same field range as the SSC magnet is used.

TABLE X. Comparison of the energy loss per cycle at 4.2 K between the C3 magnet and the SSC 50 mm aperture short model magnet. The $B_1$ range refers to the range of the dipole field during the loss measurements.

| | Unit | C3 | SSC |
|---|---|---|---|
| Conductor | [⋯] | CORC® | Nb-Ti |
| Filament size | μm | ∼1000 | 5 |
| $B_1$ range | T | 0.9–2.2 | 0.5–5.1 |
| Coupling loss | $\mathrm{J(A\,s^{-1})^{-1}\,m^{-1}}$ | 3.0 | 0.4 |
| Hysteresis loss | $\mathrm{J\,m^{-1}}$ | 187 | 67 |

Consequently, reducing the effective filament width of REBCO layer through laser striation [122–126] or aligning the REBCO tape with the local magnetic flux lines appears to be the most effective engineering approach to reducing the hysteresis loss in high-field REBCO magnet.

### C. Continue improving the performance of REBCO conductors

The C3 magnet results underscored the importance of high-performance REBCO tapes and CORC® wires. The high critical current of the commercial REBCO tape directly translated to the high performance of the CORC® wire used here. For future accelerator magnet applications, the upcoming REBCO tapes, with a thin substrate (≤ 30 μm), must be capable of sustaining a higher current density at high magnetic fields transverse to the tape's broad surface, ≥ 10 T, and at low operating temperatures ≤ 20 K. For a 8–10 T dipole magnet, the CORC® wire should carry at least 12–15 kA at 10 T, 4.2 K at a minimum bend radius of 30 mm.

Sustaining massive $\vec{I} \times \vec{B}$ forces is critical for high-field scaling. This requires advancing the mechanical integrity of REBCO tapes, understanding tape-to-core interactions in round cables, and improving overall wire bend performance. Targeting a force limit of 150 $\mathrm{kN\,m^{-1}}$ will provide the necessary margin to safely operate an 8–10 T dipole magnet.

Continued R&D on the REBCO conductor is essential to ensure future experimental magnets can demonstrate higher dipole fields.

Although striated REBCO layers are essential to suppress magnetization and hysteresis losses, we propose to prioritize this integration only after demonstrating a robust REBCO accelerator magnet that generates a 16 T steady-state dipole field at 4.2 K.

### D. Open questions

#### *1. Why did the magnet not reach the predicted dipole field of 7.3 T?*

The C3 magnet generated only 5.99 T, 81% of the short-sample prediction of 7.34 T at 8.475 kA (Fig. 4), limited by a resistive voltage of 105 μV across Layer 1. Layer 4 also developed a resistive voltage of 20 μV, inconsistent with the short-sample prediction.

Although all six layers had a critical current lower than that of the witness samples, Layers 1 and 4 had the lowest (Table VI). We suspected that the wires in both layers degraded.

Both layers indeed had issues during the coil fabrication (Sec. IV), which may have degraded the CORC® wires. If so, the electromechanical vulnerability underscored the need to handle the CORC® wire with care and to avoid straightening the bent wire as recommended by the vendor. It also illustrated a fundamental challenge for the REBCO magnet technology: once the tape is made, we have every chance to degrade it. Some margin for error in the conductor's performance is important.

In contrast to the apparent degradation in Layers 1 and 4 that can be related to the coil fabrication and handling, the CORC® wires in the remaining four layers demonstrated stable, superconducting performance up to the maximum current tested so far. Since these layers were not pushed to their absolute load-line thresholds, we cannot conclude on the ultimate performance of the wires in these layers. Testing the C3 magnet at a higher current is necessary to map out the true performance bounds of the remaining layers.

Finally, spatial variations in critical current along the continuous length of the conductor cannot be ruled out, implying that the witness samples may not perfectly represent the local performance within each layer. Validating this spatial homogeneity requires nondestructive, critical-current measurement with a high spatial resolution over the full wire length. Implementing longitudinal verification methods, such as continuous magnetic or electrical profiling frameworks [127], represents a vital quality gateway to de-risk wire performance variations prior to magnet fabrication.

#### *2. Why did the critical current of Layer 1 at 77 K decrease after the thermal cycle?*

The 77 K critical current of Layer 1 decreased by 6.3% from March to June yet showed no significant change at 4.2 K (Figs. 19 and 20). This is counterintuitive; based on the previous C2 magnet data [61], an $I_c$ degradation at 77 K should correlate with a degradation at 4.2 K, and vice versa. This suggests the critical-current drop at 77 K was not driven by the thermal cycle or the Stycast removal but by a higher bath temperature during the June test. A 0.6 K increase in the coil temperature can lead to a 6% decrease in the critical current around 77 K [128].

The measured temperature supported this conclusion. The thermometers on the aluminum shell read 0.14 K higher in the liquid nitrogen bath in June than in March. The magnet aperture was filled by liquid nitrogen in March, whereas in June, the anticryostat occupied the aperture, leaving only a 0.75 mm radial clearance. We also tracked a heat leak in the anticryostat during the 77 K test that added a thermal load to Layer 1, which was entirely absent during the 4.2 K test. Measuring the critical current at 77 K with and without the anticryostat can help clarify the issue.

#### *3. What's next?*

To determine if the REBCO technology can push the dipole field beyond 16 T, we must scale our experiments to higher fields, targeting a dipole field of 8–10 T for the next magnets. Hitting this target will unlock our next milestone and allow us to evaluate whether combining round REBCO cables with various magnet designs is effective for future high-field accelerator magnets.

Advancing this technology requires us to answer several critical questions. These include: whether we can manufacture and operate the magnets repeatedly and robustly at the target field with minimal conductor degradation, how stable and reproducible the magnetic field is alongside the magnetization effect, whether we can reliably prevent thermal runaway to protect an experimental magnet operating with stored energy approaching 100 kJ, and how we will collaborate with vendors to source next-generation conductors requiring greater length, current capacity, and mechanical strength than the baseline C3 wire.

The most effective way to solve these problems is through rapid hardware iteration: securing the conductors, making the magnets, testing them rigorously, and learning directly from the data. By sharing the C3 magnet results with the broader accelerator community, we aim to build a coalition of beta users and early adopters to accelerate the deployment of this emerging technology.

## XII. CONCLUSION

Using commercial high-current REBCO CORC® wire, the U.S. Magnet Development Program made C3, a high-temperature superconducting CCT dipole magnet. The magnet generated a 5.99 T dipole field at 4.2 K and 6.795 kA, corresponding to an overall conductor current density of 599 $\mathrm{A\,mm^{-2}}$ and a stored energy of 53 kJ. The peak electromagnetic force on the CORC® wire reached 42 $\mathrm{kN\,m^{-1}}$. Crucially, the magnet showed reproducible voltage as a function of current. The current-carrying capability showed no measurable degradation at 4.2 K following a full warm-up-cooldown thermal cycle.

Due to large REBCO filament sizes and high critical-current densities, C3 exhibited strong magnetization effects that affected field quality. The main dipole field from four consecutive current ramps showed an improving reproducibility from 0.05% at 1 T to 0.01% at 5 T.

The main field and high-order field errors, especially $b_3$ and $b_5$ showed a strong hysteresis between the up- and down-ramps of the current. The hysteresis loss was 187 J per unit magnetic length per cycle between 0.9 and 2.2 T for the C3 magnet, roughly triple that of the Nb-Ti SSC short model magnet measured from 0.5 to 5.1 T.

Despite these open challenges, the C3 magnet data showed no fundamental showstoppers preventing a CORC® CCT magnet from reaching a dipole field of 8–10 T currently dominated by Nb-Ti magnet technology. To achieve it with robust engineering margins, we are setting strict performance targets for next-generation CORC® conductors. They must carry 12–15 kA at 10 T, 4.2 K, bend to a 30 mm radius, and sustain an $\vec{I} \times \vec{B}$ force of 150 kN m$^{-1}$. Hitting these metrics requires tight, ongoing collaboration with conductor vendors.

The C3 magnet was another step toward high-field REBCO accelerator magnet technology to enhance the discovery capability of future circular colliders. We need early adopters to help develop and grow the technology.

## ACKNOWLEDGMENTS

We thank Toru Fukushima, Tetsu Tateishi, Yifei Zhang, and Drew Hazelton at SuperPower Inc. for leading the production of HM REBCO tapes used here. We thank our colleagues at LBNL for their contributions to this work: Bun Pa Lim and Kristopher Pearson for machining the mandrels; Thomas Johnson for providing the Thinky mixer for the Stycast preparation; Derek Hochvert, Simone Johnson, Chet Spencer, and James Swanson for their support during cryogenic testing; Philip Mallon for reviewing the aluminum shell designs; Rae de Leon for assisting with the magnetic measurement setup; Matthew Reynolds for installing the fiber optic sensors; Daniel Cheng for recommending Stycast 2850 FT for the interlayer gaps; and Ji Qiang for his valuable feedback on the manuscript. We thank Daniel Assell at FNAL for his craftsmanship in assembling the rotating probe for the magnetic measurements. We thank David Larbalestier, Van Griffin, James Maddox, and James Gilman at NHMFL for providing the test cryostat. We thank Kenneth Marken at the Office of High Energy Physics for valuable discussions. We also thank the fellow members of the MDP REBCO Working Group for many technical discussions: Maria Baldini, Steve Gourlay, Vadim Kashikhin, Steven Krave, Vito Lombardo, George Velev, and Xingchen Xu at FNAL and Ramesh Gupta, Mithlesh Kumar, and Vikas Teotia at Brookhaven National Laboratory. This work was supported by the U.S. MDP through Director, Office of Science, Office of High Energy Physics of the U.S. Department of Energy under Contract No. DE-AC02-05CH11231. Conductor used in this work was procured by U.S. MDP, Conductor Procurement and R&D (CPRD), supported by the Office of High Energy Physics, U.S. Department of Energy. The measurement of the wire critical current at 4.2 K at Advanced Conductor Technologies LLC was supported by MDP CPRD. The work at Advanced Conductor Technologies LLC was also supported by the Department of Energy, Office of Science, under Contract Nos. DE-SC0014009, DE-SC0018127, and DE-SC0024159.

## DATA AVAILABILITY

The data that support the findings of this article are not publicly available upon publication because it is not technically feasible and/or the cost of preparing, depositing, and hosting the data would be prohibitive within the terms of this research project. The data are available from the authors upon reasonable request.

## APPENDIX: PICTURES OF LAYER 4 INCIDENTS

Figure 31 shows where the CORC® wire was bent after derailing from the spool and catching on a nearby threaded rod. We prevented this in subsequent operations by adding a larger-diameter cover to keep the wire contained.

During Stycast curing, we rotated Layer 4 at approximately 0.3 Hz using a friction-coupled drive shaft running through the magnet aperture. The shaft was supported by rollers on one end and a drive motor on the other. A mechanical failure occurred at the motor connection, causing that end of the shaft to drop onto a vertical support stand. Prior to the incident, the lead wires at both ends of Layer 4 were rigidly clamped parallel to the shaft. As shown in Fig. 32, the drop caused the mandrel to rotate relative to the shaft, which resulted in minor bending of the lead wires.

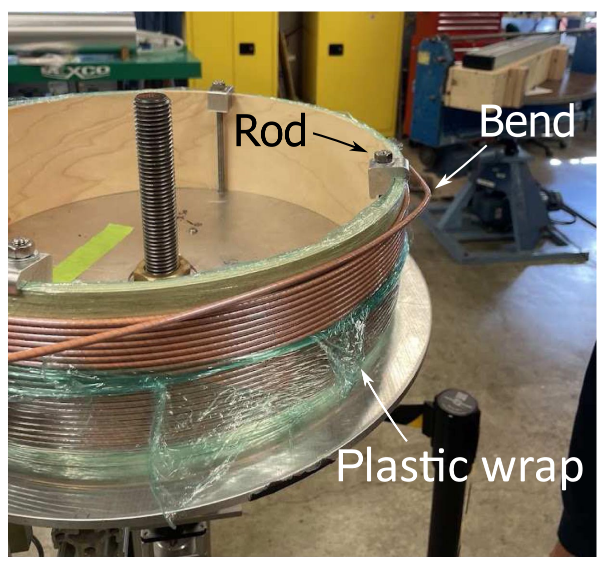


FIG. 31. Layer 4 wire came off from the top of the spool and was bent by the nearby threaded rod. The bend was partially straightened as we wrapped the CORC® wire back to the spool.

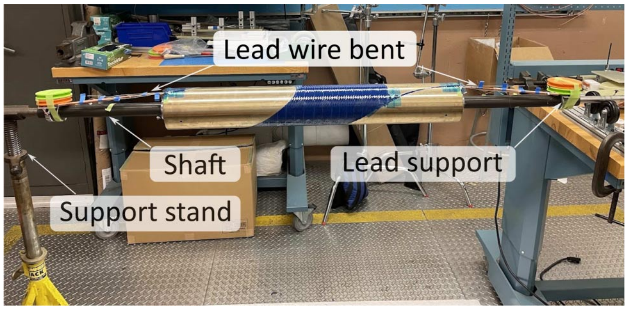


FIG. 32. The lead wire at both ends of Layer 4 slightly bent after the mandrel fell and was arrested by the vertical support stand. The lead wires were parallel to the shaft before the incident.


[1] R. Palmer and A. V. Tollestrup, Superconducting magnet technology for accelerators, Annu. Rev. Nucl. Part. Sci. **34**, 247 (1984).

[2] A. Tollestrup and E. Todesco, The development of superconducting magnets for use in particle accelerators: From the Tevatron to the LHC, Rev. Accel. Sci. Techol. **01**, 185 (2008).

[3] L. Rossi and L. Bottura, Superconducting magnets for particle accelerators, Rev. Accel. Sci. Techol. **5**, 51 (2012).

[4] L. Bottura, S. A. Gourlay, A. Yamamoto, and A. V. Zlobin, Superconducting magnets for particle accelerators, IEEE Trans. Nucl. Sci. **63**, 751 (2016).

[5] L. Rossi, Superconductivity: Its role, its success and its setbacks in the large hadron collider of CERN, Supercond. Sci. Technol. **23**, 034001 (2010).

[6] E. Todesco *et al.*, The high luminosity LHC interaction region magnets towards series production, Supercond. Sci. Technol. **34**, 053001 (2021).

[7] G. Ambrosio and P. Ferracin, Large-aperture high-field $Nb_3Sn$ quadrupole magnets for HiLumi, in *The Future of the Large Hadron Collider* (World Scientific, Singapore, 2023), pp. 121–133.

[8] G. L. Sabbi, High-field magnets for future hadron colliders, Annu. Rev. Nucl. Part. Sci. **74**, 389 (2024).

[9] E. Todesco, Status and perspectives of high field magnets for particle accelerators, IEEE Trans. Appl. Supercond. **35**, 1 (2025).

[10] R. M. Scanlan, A. P. Malozemoff, and D. C. Larbalestier, Superconducting materials for large scale applications, Proceed. IEEE **92**, 1639 (2004).

[11] M. Leroux, F. F. Balakirev, M. Miura, K. Agatsuma, L. Civale, and B. Maiorov, Dynamics and critical currents in fast superconducting vortices at high pulsed magnetic fields, Phys. Rev. Appl. **11**, 054005 (2019).

[12] D. Uglietti, A review of commercial high temperature superconducting materials for large magnets: From wires and tapes to cables and conductors, Supercond. Sci. Technol. **32**, 053001 (2019), and references therein.

[13] A. Godeke, High temperature superconductors for commercial magnets, Supercond. Sci. Technol. **36**, 113001 (2023).

[14] Maglab sets a new world record magnetic field (2025). https://nationalmaglab.org/news-events/news/a-prototype-miniature-superconducting-magnet/.

[15] S. Hahn, K. Kim, K. Kim, X. Hu, T. Painter, I. Dixon, S. Kim, K. R. Bhattarai, S. Noguchi, J. Jaroszynski, and D. C. Larbalestier, 45.5-tesla direct-current magnetic field generated with a high-temperature superconducting magnet, Nature (London) **570**, 496 (2019).

[16] P. McIntyre and A. Sattarov, On the feasibility of a tripler upgrade for LHC, in *Second CARE-HHH-APD Workshop on Scenarios for the LHC Luminosity Upgrade* (CERN, Meyrin, Switzerland, 2006), pp. 107–110.

[17] A. Godeke, D. Cheng, D. R. Dietderich, P. Ferracin, S. O. Prestemon, G. Sabbi, and R. M. Scanlan, Limits of NbTi and $Nb_3Sn$, and development of W&R Bi-2212 high field accelerator magnets, IEEE Trans. Appl. Supercond. **17**, 1149 (2007).

[18] L. Bottura, Magnets for future colliders: The muon collider as a case study, in *Proceedings of the Joint Universities Accelerator School (JUAS): Courses and Exercises*, edited by E. Métral (CERN Yellow Reports: School Proceedings, 2024), Vol. 3, pp. 2179–2200.

[19] D. G. Whyte, J. Minervini, B. LaBombard, E. Marmar, L. Bromberg, and M. Greenwald, Smaller & sooner: Exploiting high magnetic fields from new superconductors for a more attractive fusion energy development path, J. Fusion Energy **35**, 41 (2016).

[20] Z. S. Hartwig *et al.*, The SPARC toroidal field model coil program, IEEE Trans. Appl. Supercond. **34**, 0600316 (2024).

[21] R. Gupta, M. Anerella, J. Cozzolino, P. Joshi, W. Sampson, P. Wanderer, and A. Zeller, HTS quadrupole for FRIB–design, construction and test results, IEEE Trans. Appl. Supercond. **25**, 4603306 (2015).

[22] K. Tsuchiya, M. Tawada, M. Masuzawa, A. Terashima, N. Ohuchi, M. Sugano, X. Wang, A. Kikuchi, Y. Arimoto, Z. Zong, S. Fujita, M. Daibo, and Y. Iijima, Development of HTS sextupole magnet for SuperKEKB interaction region, IEEE Trans. Appl. Supercond. **26**, 4100904 (2016).

[23] N. Zangenberg, G. Nielsen, N. Hauge, B. R. Nielsen, A. Baurichter, C. G. Pedersen, L. Brauner, B. Ulsoe, and S. P. Moller, Conduction cooled high temperature superconducting dipole magnet for accelerator applications, IEEE Trans. Appl. Supercond. **22**, 4004004 (2012).

[24] N. Amemiya, S. Inoue, X. Luo, Y. Sogabe, S. Takayama, Y. Ishii, T. Ogitsu, Y. Iwata, K. Noda, and M. Yoshimoto, Test of cryocooler-cooled RE-123 magnet on HIMAC beam line in S-innovation program, IEEE Trans. Appl. Supercond. **29**, 4600305 (2019).

[25] G. Kim, J. Park, W. Jung, H. Park, Y. Yan, J. Kim, H. Yang, M. Ahn, J. Bang, G. Hahn, S. Choi, H. Kang, and S. Hahn, Field uniformity enhancement in a prototype high-temperature superconducting dipole magnet, Sci. Rep. **16**, 3589 (2026).

[26] S. Asai *et al.*, Exploring the quantum universe: Pathways to innovation and discovery in particle physics, Tech. Rep. (Particle Physics Project Prioritization Panel, 2024).

[27] K. Marken, Fundamental issues in high temperature superconductor (HTS) materials science and engineering, in *High Temperature Superconductors (HTS) for Energy Applications*, Woodhead Publishing Series in Energy, edited by Z. Melhem (Woodhead Publishing, 2012), p. 33.

[28] L. Rossi and A. V. Zlobin, $Nb_3Sn$ accelerator magnets: The early days (1960s–1980s), in *$Nb_3Sn$ Accelerator Magnets: Designs, Technologies and Performance*, edited by D. Schoerling and A. V. Zlobin (Springer International Publishing, Cham, 2019), p. 84.

[29] N. Amemiya, K. Goda, H. Otake, T. Nakamura, T. Ogitsu, K. Koyanagi, T. Kurusu, Y. Mori, Y. Iwata, K. Noda, and M. Yoshimoto, Progress of research and development of fundamental technologies for accelerator magnets using coated conductors, IEEE Trans. Appl. Supercond. **23**, 4601905 (2013).

[30] R. Gupta, M. Anerella, A. Ghosh, S. L. Lalitha, W. Sampson, J. Schmalzle, J. Kolonko, R. Scanlan, R. Weggel, E. Willen, and K. Nakao, Hybrid high-field cosine-theta accelerator magnet R&D with second-generation HTS, IEEE Trans. Appl. Supercond. **25**, 4003704 (2015).

[31] K. Koyanagi, S. Takayama, H. Miyazaki, T. Tosaka, K. Tasaki, T. Kurusu, and Y. Ishii, Development of saddle-shaped coils for accelerator magnets wound with YBCO-coated conductors, IEEE Trans. Appl. Supercond. **25**, 4003104 (2015).

[32] H. Maeda and Y. Yanagisawa, Recent developments in high-temperature superconducting magnet technology (review), IEEE Trans. Appl. Supercond. **24**, 4602412 (2014).

[33] G. de Rijk, The EuCARD high field magnet project, IEEE Trans. Appl. Supercond. **22**, 4301204 (2012).

[34] L. Rossi *et al.*, The EuCARD-2 future magnets European collaboration for accelerator-quality HTS magnets, IEEE Trans. Appl. Supercond. **25**, 4001007 (2015).

[35] L. Rossi and C. Senatore, HTS accelerator magnet and conductor development in Europe, Instruments **5**, 8 (2021).

[36] B. Auchmann, E. Todesco, A. Ballarino, N. Bagrets, A. Milanese, E. Rochepault, L. Rossi, C. Senatore, and F. Toral, High field magnet programme—European strategy input, arXiv:2504.16885.

[37] M. Durante, F. Borgnolutti, D. Bouziat, P. Fazilleau, J.-M. Gheller, F. Molinie, and P. De Antoni, Realization and first test results of the EuCARD 5.4-T REBCO dipole magnet, IEEE Trans. Appl. Supercond. **28**, 4203805 (2018).

[38] M. Durante, P. Fazilleau, T. Lecrevisse, C. Lorin, M. Segreti, and O. Tellier, Overview of HTS accelerator magnet developments at CEA Saclay, IEEE Trans. Appl. Supercond. **34**, 4002905 (2024).

[39] G. A. Kirby *et al.*, Accelerator-quality HTS dipole magnet demonstrator designs for the EuCARD-2 5-T 40-mm clear aperture magnet, IEEE Trans. Appl. Supercond. **25**, 4000805 (2015).

[40] J. van Nugteren *et al.*, Powering of an HTS dipole insert-magnet operated standalone in helium gas between 5 and 85 K, Supercond. Sci. Technol. **31**, 065002 (2018).

[41] M. Durante, C. Lorin, T. Lecrevisse, M. Segreti, G. Kirby, and J. Van Nugteren, Manufacturing of the EuCARD2 Roebel-based cos-theta coils at CEA Saclay, IEEE Trans. Appl. Supercond. **30**, 4602505 (2020).

[42] A. Baskys, A. Ballarino, C. Barth, L. Fiscarelli, N. Gal, F. J. Mangiarotti, J. Mazet, D. Perini, and A. Saba, Development and testing of the first REBCO racetrack model coils at CERN, IEEE Trans. Appl. Supercond. **36**, 4003306 (2026).

[43] HFM forum: Test results of ROCCO, an HTS common coil demonstrator (2026), https://indico.cern.ch/event/1638824/.

[44] Z. Xu, Y. Liu, J. Lu, P. Song, Y. Zhang, M. Xiao, C. Xin, L. Shao, C. Korte, X. Kang, M. Guan, and T. Qu, Test results and analysis of a 5 T/34 mm REBCO dipole magnet insert at 4.2 K, IEEE Trans. Appl. Supercond. **36**, 4601005 (2026).

[45] Q. Xu, Overview of HTS conductor and magnet development in China, https://indico.cern.ch/event/1455509/contributions/6709870/ (2025), accessed: 2026-2-2.

[46] T. Lecrevisse, E. Benoist, A. Blondelle, A. Caunes, M. Durochat, C. Genot, G. Lenoir, B. Maloeuvre, A. Ballarino, and A. Baskys, Metal as insulation REBCO racetracks coils: Development, fabrication, and cryogenic testing at CEA Paris-Saclay, IEEE Trans. Appl. Supercond. **36**, 4001405 (2026).

[47] S. A. Gourlay, S. O. Prestemon, A. V. Zlobin, L. Cooley, and D. Larbalestier, The U.S. magnet development program plan, https://escholarship.org/uc/item/5178744r (2016).

[48] L. Cooley *et al.*, The 2025 roadmaps for the US magnet development program, arXiv:2508.19220.

[49] D. Larbalestier, Status of Bi-2212 conductor and coil technology, 1st High Temperature superconductors for Accelerator Technology (HiTAT) workshop (2023), https://indico.cern.ch/event/1220254/contributions/5270812/.

[50] T. Shen, E. Bosque, D. Davis, J. Jiang, M. White, K. Zhang, H. Higley, M. Turqueti, Y. Huang, H. Miao, U. Trociewitz, E. Hellstrom, J. Parrell, A. Hunt, S. Gourlay, S. Prestemon, and D. Larbalestier, Stable, predictable and training-free operation of superconducting Bi-2212 Rutherford cable racetrack coils at the wire current density of 1000 $A/mm^2$, Sci. Rep. **9**, 10170 (2019).

[51] T. Shen and L. Garcia Fajardo, Superconducting accelerator magnets based on high-temperature superconducting Bi-2212 round wires, Instruments **4**, 17 (2020).

[52] D. C. van der Laan, J. D. Weiss, and D. M. McRae, Status of CORC® cables and wires for use in high-field magnets and power systems a decade after their introduction, Supercond. Sci. Technol. **32**, 033001 (2019).

[53] S. Kar, J. S. Sandra, W. Luo, M. Kochat, J. Jaroszynski, D. Abraimov, G. Majkic, and V. Selvamanickam, Next-generation highly flexible round REBCO STAR wires with over 580 $A\,mm^{-2}$ at 4.2 K, 20 T for future compact magnets, Supercond. Sci. Technol. **32**, 10LT01 (2019).

[54] V. V. Kashikhin *et al.*, Re-assembly and test of a COMB dipole magnet with STAR wires, IEEE Trans. Appl. Supercond. **35**, 4000607 (2025).

[55] L. Brouwer, Y. Yan, X. Wang, J. F. Croteau, P. Ferracin, J. L. R. Fernandez, and A. Saravanan, Elliptic aperture CCT coils for HTS dipole magnets, IEEE Trans. Appl. Supercond. **36**, 4600107 (2026).

[56] J. L. Rudeiros Fernández and P. Ferracin, Uni-layer magnets: A new concept for LTS and HTS based superconducting magnets, Supercond. Sci. Technol. **36**, 055003 (2023).

[57] D. Cuneo, J. L. Rudeiros Fernández, P. Ferracin, P. Arpaia, L. Brouwer, J.-F. Croteau, M. D'Addazio, A. Esposito, H. Higley, M. Marchevsky, A. Saravanan, X. Wang, and Y. Yan, Development and testing of the first HTS uni-layer magnet prototype (2025).

[58] H. G. Khodzhibagiyan, V. D. Kekelidze, G. Kuznetsov, A. Merkuriev, D. N. Nikiforov, M. Novikov, and G. V. Trubnikov, Quadrupole superconducting model magnet for upgrade of the nuclotron synchrotron, IEEE Trans. Appl. Supercond. **32**, 4003704 (2022).

[59] L. Fan, P. Song, M. Xiao, L. Shao, F. Feng, M. Guan, and T. Qu, Design and testing of a prototype canted-cosine-theta HTS dipole magnet using CORC cable, IEEE Trans. Appl. Supercond. **34**, 4600605 (2024).

[60] X. Wang, D. R. Dietderich, J. DiMarco, W. B. Ghiorso, S. A. Gourlay, H. C. Higley, A. Lin, S. O. Prestemon, D. van der Laan, and J. D. Weiss, A 1.2 T canted cos$\theta$ dipole magnet using high-temperature superconducting CORC® wires, Supercond. Sci. Technol. **32**, 075002 (2019).

[61] X. Wang *et al.*, Development and performance of a 2.9 Tesla dipole magnet using high-temperature superconducting CORC® wires, Supercond. Sci. Technol. **34**, 015012 (2020).

[62] D. van der Laan, J. Weiss, K. Radcliff, and D. Abraimov, CORC® wires allowing bending to 20 mm radius with 97.5% retention in critical current and having an engineering current density of 530 A/mm$^2$ at 20 T, Supercond. Sci. Technol. **37**, 115007 (2024).

[63] D. Abraimov *et al.*, Fabrication and test of C3a: A six-layer subscale canted cos$\theta$ dipole magnet using high-temperature superconducting CORC wires, IEEE Trans. Appl. Supercond. **35**, 4004115 (2025).

[64] S. Caspi and P. Ferracin, Limits of $Nb_3Sn$ accelerator magnets, in *Proceedings of 2005 Particle Accelerator Conference* (2005), pp. 107–111.

[65] L. Rossi and E. Todesco, Electromagnetic design of superconducting dipoles based on sector coils, Phys. Rev. ST Accel. Beams **10**, 112401 (2007).

[66] D. I. Meyer and R. Flasck, A new configuration for a dipole magnet for use in high energy physics applications, Nucl. Instrum. Methods **80**, 339 (1970).

[67] A. V. Gavrilin, M. D. Bird, S. T. Bole, and Y. M. Eyssa, Conceptual design of high transverse field magnets at the NHMFL, IEEE Trans. Appl. Supercond. **12**, 465 (2002).

[68] C. L. Goodzeit, M. J. Ball, and R. B. Meinke, The double-helix dipole—A novel approach to accelerator magnet design, IEEE Trans. Appl. Supercond. **13**, 1365 (2003).

[69] J. H. Rochford, D. E. Baynham, and A. Devred, An evaluation of the helical winding method applied to the next European dipole project, IEEE Trans. Appl. Supercond. **18**, 1541 (2008).

[70] S. Caspi, F. Borgnolutti, L. Brouwer, D. Cheng, D. R. Dietderich, H. Felice, A. Godeke, R. Hafalia, M. Martchevskii, S. Prestemon, E. Rochepault, C. Swenson, and X. Wang, Canted–Cosine–Theta magnet (CCT)—A concept for high field accelerator magnets, IEEE Trans. Appl. Supercond. **24**, 4001804 (2014).

[71] L. Quéval and R. Gottkehaskamp, Analytical field calculation of modulated double helical coils, IEEE Trans. Appl. Supercond. **25**, 4901307 (2015).

[72] L. N. Brouwer, Canted-Cosine-Theta Superconducting Accelerator Magnets for High Energy Physics and Ion Beam Cancer Therapy, Ph.D. thesis, University of California, Berkeley, 2015.

[73] S. Farinon and R. Musenich, Biot–Savart approach to analytical computation of magnetic fields and forces of CCT magnets, IEEE Trans. Appl. Supercond. **31**, 4900308 (2021).

[74] L. Brouwer, Producing circular field harmonics inside elliptic magnet apertures with superconducting canted-cosine-theta coils, Phys. Rev. Accel. Beams **27**, 022402 (2024).

[75] J. Li, K. Wang, K. Wang, X. Zhang, S. Cai, X. Yan, and K. Zhu, Generation of circular field harmonics in quasipolygonal magnet apertures using superconducting canted cosine-theta coils, Phys. Rev. Accel. Beams **28**, 052401 (2025).

[76] Y. Yang, S. Caspi, and L. Brouwer, Analytical expression of a finite, long, conical canted-cosine-theta coil for particle collider interaction regions, Phys. Rev. Accel. Beams **28**, 102401 (2025).

[77] B. Auchmann, D. M. Araujo, A. Brem, M. Daly, R. Felder, J. Feuvrier, C. Hug, O. Kirby, F. Mangiarotti, A. Milanese, G. Montenero, G. Rolando, S. Sanfilippo, and S. Sidorov, Test results from CD1 short CCT $Nb_3Sn$ dipole demonstrator and considerations about CCT technology for the FCC-hh main dipole, IEEE Trans. Appl. Supercond. **34**, 4000906 (2024).

[78] L. Brouwer, S. Caspi, R. Hafalia, A. Hodgkinson, S. Prestemon, D. Robin, and W. Wan, Design of an achromatic superconducting magnet for a proton therapy gantry, IEEE Trans. Appl. Supercond. **27**, 4400106 (2017).

[79] A. Haziot, G. Kirby, A. Dallocchio, A. Devred, A. Foussat, L. Gentini, F. J. Mangiarotti, M. Pentella, C. Petrone, F.-O. Pincot, J.-S. Rigaud, and J. Guardia-Valenzuela, Curved-canted-cosine-theta (CCCT) dipole prototype development at CERN, IEEE Trans. Appl. Supercond. **34**, 4002608 (2024).

[80] J. L. Rudeiros Fernández, P. Ferracin, D. Arbelaez, D. Cuneo, S. Prestemon, and X. Wang, Development of the first HTS demonstrator based on the uni-layer concept, *Presentation at the Applied Superconductivity Conference, Salt Lake City, U.S.A* (2024).

[81] A. Godeke, L. N. Brouwer, S. Caspi, D. R. Dietderich, S. A. Gourlay, R. R. Hafalia, N. I. Heys, H. C. Higley, T. M. Lipton, M. A. Reynolds, and J. H. Swanson, Bi-2212 canted-cosine-theta coils for high-field accelerator magnets, IEEE Trans. Appl. Supercond. **25**, 4002404 (2015).

[82] L. Garcia Fajardo, L. Brouwer, S. Caspi, S. Gourlay, S. Prestemon, and T. Shen, Designs and prospects of Bi-2212 canted-cosine-theta magnets to increase the magnetic field of accelerator dipoles beyond 15 T, IEEE Trans. Appl. Supercond. **28**, 4008305 (2018).

[83] T. Shen *et al.*, Design, fabrication, and characterization of a high-field high-temperature superconducting Bi-2212 accelerator dipole magnet, Phys. Rev. Accel. Beams. **25**, 122401 (2022).

[84] B. Auchmann, L. Brouwer, S. Caspi, J. Gao, G. Montenero, M. Negrazus, G. Rolando, and S. Sanfilippo, Electromechanical design of a 16-T CCT Twin-Aperture dipole for FCC, IEEE Trans. Appl. Supercond. **28**, 4000705 (2018).

[85] D. Arbelaez, T. Bogdanof, L. Brouwer, S. Caspi, D. Dietderich, J. L. R. Fernández, P. Ferracin, S. Gourlay, R. Hafalia, M. Krutulis, M. Marchevsky, M. Maruszewski, C. Myers, S. Prestemon, M. Reynolds, T. Shen, J. Swanson, R. Teyber, M. Turqueti, G. Vallone, and X. Wang, Status of the $Nb_3Sn$ Canted-Cosine-Theta dipole magnet program at Lawrence Berkeley National Laboratory, IEEE Trans. Appl. Supercond. **32**, 4003207 (2022).

[86] D. Arbelaez, R. Teyber, J. L. Rudeiros Fernández, L. Brouwer, G. Vallone, M. Marchevsky, M. Turqueti, I. Pong, J.-F. Croteau, M. Naus, S. Caspi, P. Ferracin, and S. Prestemon, Training-free demonstration of a 5.4 T $Nb_3Sn$ Canted–Cosine–Theta accelerator dipole impregnated with paraffin wax, Supercond. Sci. Technol. **37**, 065015 (2024).

[87] H. Witte, T. Yokoi, S. L. Sheehy, K. Peach, S. Pattalwar, T. Jones, J. Strachan, and N. Bliss, The advantages and challenges of helical coils for small accelerators—A case study, IEEE Trans. Appl. Supercond. **22**, 4100110 (2012).

[88] L. Brouwer, S. Caspi, K. Edwards, A. Godeke, R. Hafalia, A. Hodgkinson, A. Huggins, C. Myers, S. Myers, M. Schillo, J. Taylor, M. Turqueti, X. Wang, W. Wan, and S. Prestemon, Design and test of a curved superconducting dipole magnet for proton therapy, Nucl. Instrum. Methods Phys. Res. Sect. A **957**, 163414 (2020).

[89] X. Zhang, W. Yang, Y. Liang, L. Ma, W. You, E. Mei, X. Ou, Y. Tong, D. Ni, J. Lu, B. Bai, Y. Yang, X. Qin, and W. Wu, Design and test of a curved canted–cosine–theta superconducting dipole magnet for next generation ion therapy, IEEE Trans. Appl. Supercond. **33**, 4401507 (2023).

[90] G. A. Kirby, L. Gentini, J. Mazet, M. Mentink, F. Mangiarotti, J. Van Nugteren, J. S. Murtomäki, P. Hagen, F. O. Pincot, N. Bourcey, J. C. Perez, G. D. Rijk, E. Todesco, and J. Rysti, Hi-Lumi LHC twin aperture orbit correctors 0.5-m model magnet development and cold test, IEEE Trans. Appl. Supercond. **28**, 4002205 (2018).

[91] W. Wu, Y. Liang, L.-C. Zhou, E.-M. Mei, D.-S. Ni, S.-J. Zhen, X.-J. Ou, and W.-J. Yang, Multipole magnets for the HIAF fragment separator using the Canted-Cosine-Theta (CCT) geometry, J. phys. Conf. Ser. **1401**, 012015 (2020).

[92] J. Weiss, D. van der Laan, T. Mulder, H. T. Kate, A. Godeke, D. Kolb-Bond, and D. Larbalestier, Enhanced flexibility of round high-temperature superconducting CORC wires for high-field magnet applications, *Presentation at the 8th Workshop on Mechanical and Electromagnetic Properties of Composite Superconductors (MEM16)* (2016), https://www.advancedconductor.com/wp-content/uploads/2026/02/Weiss-MEM-2016.pdf.

[93] https://www.youtube.com/shorts/pfLZNk--SWY.

[94] T. Lipton, Magnet trepanning tool P1 (2025), https://www.youtube.com/watch?v=TnFoz3zuO4s.

[95] J. DiMarco, G. Chlachidze, A. Makulski, D. Orris, M. Tartaglia, J. C. Tompkins, G. V. Velev, and X. Wang, Application of PCB and FDM technologies to magnetic measurement probe system development, IEEE Trans. Appl. Supercond. **23**, 9000505 (2013).

[96] L. Luo, P. Ferracin, H. Higley, M. Marchevsky, S. Prestemon, J. L. Rudeiros Fernández, R. Teyber, M. Turqueti, G. Vallone, X. Wang, and Y. Wu, Distributed fiber-optic sensing in a subscale high-temperature superconducting dipole magnet, Supercond. Sci. Technol. **38**, 035029 (2025).

[97] L. Bottura, Standard analysis procedures for field quality measurement of the LHC magnets—Part I: Harmonics, Tech. Report No. LHC-MTA-IN-97-007 (LHC/MTA, 2001).

[98] N. J. Sammut, L. Bottura, P. Bauer, G. Velev, T. Pieloni, and J. Micallef, Mathematical formulation to predict the harmonics of the superconducting Large Hadron Collider magnets. II. Dynamic field changes and scaling laws, Phys. Rev. ST Accel. Beams **10**, 082802 (2007).

[99] J. P. Ozelis, S. Delchamps, S. Gourlay, T. Jaffery, W. Kinney, W. Koska, M. Kuchnir, M. J. Lamm, P. O. Mazur, D. Orris, J. Strait, M. Wake, J. Dimarco, J. Kuzminski, and H. Zheng, AC loss measurements of model and full size 50 mm SSC collider dipole magnets at Fermilab, IEEE Trans. Appl. Supercond. **3**, 678 (1993).

[100] A. P. Verweij, D. Leroy, L. Walckiers, R. Wolf, and H. H. J. ten Kate, Analysis of the AC loss measurements on the one-metre dipole model magnets for the CERN LHC, IEEE Trans. Magn. **30**, 1758 (1994).

[101] N. Amemiya, Z. Zhang, T. Sano, Y. Sogabe, T. Ogitsu, K. Koyanagi, T. Kurusu, Y. Mori, Y. Iwata, K. Noda, and M. Yoshimoto, Progress of fundamental technology R&D toward accelerator magnets using coated conductors in S-Innovation program, IEEE Trans. Appl. Supercond. **25**, 4003505 (2015).

[102] H. Reymond, M. Dam, H. Felice, A. Haziot, P. Jankowski, P. Koziol, T. Nes, F. Pincot, and S. Richter, Development of an automated high temperature superconductor coil winding machine at CERN, in *Proceedings of the 18th International Conference on Accelerator and Large Experimental Physics Control Systems* (JACoW Publishing, Geneva, Switzerland, 2022).

[103] M. Dam and T. Arndt, Robotic winding of non-planar high-temperature superconducting coils, Supercond. Sci. Technol. **38**, 125004 (2025).

[104] J. Stern, J. Swanson, T. Bogdanof, M. Krutulis, J. Weiss, D. van der Laan, X. Wang, and L. Chiesa, Developing a vacuum pressure impregnation procedure for CORC wires, IEEE Trans. Appl. Supercond. **32**, 4800904 (2022).

[105] J. L. Rudeiros Fernández, D. Arbelaez, L. Brouwer, S. Caspi, P. Ferracin, R. Hafalia, M. Krutulis, S. Prestemon, M. A. Reynolds, T. Shen, J. H. Swanson, and G. Vallone, Assembly and mechanical analysis of the canted-cosine-theta subscale magnets, IEEE Trans. Appl. Supercond. **27**, 4006505 (2022).
[106] M. Marchevsky, Quench detection and protection for high-temperature superconductor accelerator magnets, Instruments **5**, 27 (2021).
[107] R. Teyber, J. Weiss, M. Marchevsky, S. Prestemon, and D. van der Laan, Current distribution monitoring enables quench and damage detection in superconducting fusion magnets, Sci. Rep. **12**, 22503 (2022).
[108] F. Scurti, S. Ishmael, G. Flanagan, and J. Schwartz, Quench detection for high temperature superconductor magnets: A novel technique based on Rayleigh-back-scattering interrogated optical fibers, Supercond. Sci. Technol. **29**, 03LT01 (2016).
[109] L. Luo, P. Ferracin, J. Stern, D. Van der Laan, X. Wang, J. Weiss, and Y. Wu, Distributed fiber optic sensing to identify locations of resistive transitions in REBCO conductors and magnets, IEEE Trans. Appl. Supercond. **32**, 9000906 (2022).
[110] M. Marchevsky and S. Prestemon, Distributed thermometry for superconducting magnets using non-leaky acoustic waveguides, Supercond. Sci. Technol. **36**, 045005 (2023).
[111] D. C. van der Laan, D. M. McRae, and J. D. Weiss, Effect of transverse compressive monotonic and cyclic loading on the performance of superconducting CORC® cables and wires, Supercond. Sci. Technol. **32**, 015002 (2018).
[112] X. Xu, F. Wan, S. Cohan, and V. V. Kashikhin, Critical transverse compressive stresses of straight and bent CORC® wires with and without impregnation, Supercond. Sci. Technol. **39**, 045008 (2026).
[113] E. Todesco, L. Bottura, M. Giovannozzi, P. Hagen, M. Juchno, M. Lamont, E. Maclean, M. Schaumann, F. Schmidt, M. Solfaroli Camillocci, R. Tomas Garcia, and J. Wenninger, The magnetic behaviour of the LHC at 6.5 TeV, IEEE Trans. Appl. Supercond. **26**, 4005707 (2016).
[114] C. Petrone, J. van Nugteren, H. Bajas, L. Bottura, G. Kirby, L. Rossi, and S. Russenschuck, Measurement and analysis of the dynamic effects in an HTS dipole magnet, IEEE Trans. Appl. Supercond. **28**, 4604404 (2018).
[115] K. Suzuki, T. Ogitsu, Y. Ishii, K. Koyanagi, S. Takayama, K. Tasaki, and N. Amemiya, Field quality measurement of an HTS magnet for a rotating gantry, IEEE Trans. Appl. Supercond. **27**, 4600405 (2017).
[116] K.-H. Mess, P. Schmüser, and S. Wolff, *Superconducting accelerator magnets* (World Scientific, Singapore, 1996).
[117] C. S. Myers, M. D. Sumption, and E. W. Collings, Magnetization and flux penetration of YBCO CORC cable segments at the injection fields of accelerator magnets, IEEE Trans. Appl. Supercond. **29**, 4701105 (2019).
[118] Y. Yan, Design study of LPF3 dipole magnet (2020).
[119] Y. Yanagisawa, Y. Xu, X. Jin, H. Nakagome, and H. Maeda, Reduction of screening current-induced magnetic field of REBCO coils by the use of multi-filamentary tapes, IEEE Trans. Appl. Supercond. **25**, 6603705 (2015).
[120] M. Green, Control of the fields due to superconductor magnetization in the SSC magnets, IEEE Trans. Magn. **23**, 506 (1987).
[121] R. C. Gupta, S. A. Kahn, and G. H. Morgan, SSC 50 mm dipole cross section, in *Supercollider 3* (Springer US, Boston, MA, 1991), pp. 587–599.
[122] I. Kesgin, G. A. Levin, T. J. Haugan, and V. Selvamanickam, Multifilament, copper-stabilized superconductor tapes with low alternating current loss, Appl. Phys. Lett. **103**, 252603 (2013).
[123] M. Vojenčiak, A. Kario, B. Ringsdorf, R. Nast, D. C. van der Laan, J. Scheiter, A. Jung, B. Runtsch, F. Gömöry, and W. Goldacker, Magnetization ac loss reduction in HTS CORC® cables made of striated coated conductors, Supercond. Sci. Technol. **28**, 104006 (2015).
[124] F. Grilli and A. Kario, How filaments can reduce AC losses in HTS coated conductors: a review, Supercond. Sci. Technol. **29**, 083002 (2016).
[125] N. Amemiya, M. Shigemasa, A. Takahashi, N. Wang, Y. Sogabe, S. Yamano, and H. Sakamoto, Effective reduction of magnetisation losses in copper-plated multifilament coated conductors using spiral geometry, Supercond. Sci. Technol. **35**, 025003 (2022).
[126] N. Amemiya, Y. Sogabe, M. Shigemasa, H. Uegaki, and S. Sonobe, SCSC-IFB cable: A novel low-AC-loss cable composed of multifilament coated conductors with superconducting inter-filament bridges, Supercond. Sci. Technol. **39**, 045010 (2026).
[127] L. Lai, K. Zhao, Y. Yue, and C. Gu, Design and prototype testing of a contactless HTS cable measurement system, Supercond. Sci. Technol. **38**, 045012 (2025).
[128] D. C. van der Laan, J. D. Weiss, C. H. Kim, L. Graber, and S. Pamidi, Development of CORC® cables for helium gas cooled power transmission and fault current limiting applications, Supercond. Sci. Technol. **31**, 085011 (2018).